National Library of Canada
Bibliothèque nationale du Canada

Canadian Theses Service
Service des thèses canadiennes

Ottawa, Canada
K1A 0N4

NOTICE

The quality of this microform is heavily dependent upon the quality of the original thesis submitted for microfilming. Every effort has been made to ensure the highest quality of reproduction possible.

If pages are missing, contact the university which granted the degree.

Some pages may have indistinct print especially if the original pages were typed with a poor typewriter ribbon or if the university sent us an inferior photocopy.

Reproduction in full or in part of this microform is governed by the Canadian Copyright Act, R.S.C. 1970, c. C-30, and subsequent amendments.

AVIS

La qualité de cette microforme dépend grandement de la qualité de la thèse soumise au microfilmage. Nous avons tout fait pour assurer une qualité supérieure de reproduction.

S'il manque des pages, veuillez communiquer avec l'université qui a conféré le grade.

La qualité d'impression de certaines pages peut laisser à désirer, surtout si les pages originales ont été dactylographiées à l'aide d'un ruban usé ou si l'université nous a fait parvenir une photocopie de qualité inférieure.

La reproduction, même partielle, de cette microforme est soumise à la Loi canadienne sur le droit d'auteur, SRC 1970, c. C-30, et ses amendements subséquents.

NL-339 (r. 88/04) c

Canada

UNIVERSITY OF ALBERTA

FACULTY OF GRADUATE STUDIES AND RESEARCH

BEAM-LASER LIFETIME MEASUREMENTS FOR THE 3P LEVELS OF Mg II

BY

YANMIN LI

©

A THESIS

SUBMITTED TO THE FACULTY OF GRADUATE STUDIES AND RESEARCH

IN PARTIAL FULFILLMENT OF THE REQUIREMENTS FOR THE DEGREE

OF MASTER OF SCIENCE

IN

ASTROPHYSICS

DEPARTMENT OF PHYSICS

EDMONTON, ALBERTA

SPRING 1990

National Library of Canada
Bibliothèque nationale du Canada

Canadian Theses Service
Service des thèses canadiennes

Ottawa, Canada
K1A 0N4

NOTICE

The quality of this microform is heavily dependent upon the quality of the original thesis submitted for microfilming. Every effort has been made to ensure the highest quality of reproduction possible.

If pages are missing, contact the university which granted the degree.

Some pages may have indistinct print especially if the original pages were typed with a poor typewriter ribbon or if the university sent us an inferior photocopy.

Reproduction in full or in part of this microform is governed by the Canadian Copyright Act, R.S.C. 1970, c. C-30, and subsequent amendments.

AVIS

La qualité de cette microforme dépend grandement de la qualité de la thèse soumise au microfilmage. Nous avons tout fait pour assurer une qualité supérieure de reproduction.

S'il manque des pages, veuillez communiquer avec l'université qui a conféré le grade.

La qualité d'impression de certaines pages peut laisser à désirer, surtout si les pages originales ont été dactylographiées à l'aide d'un ruban usé ou si l'université nous a fait parvenir une photocopie de qualité inférieure.

La reproduction, même partielle, de cette microforme est soumise à la Loi canadienne sur le droit d'auteur, SRC 1970, c. C-30, et ses amendements subséquents.

ISBN 0-315-60241-4

NL-339 (r. 88/04) c

Canada

UNIVERSITY OF ALBERTA

RELEASE FORM

NAME OF AUTHOR: **YANMIN LI**

TITLE OF THESIS: **BEAM-LASER LIFETIME MEASUREMENTS FOR THE 3P LEVELS OF Mg II**

DEGREE: **MASTER OF SCIENCE**

YEAR THIS DEGREE GRANTED: **1990**

PERMISSION IS HEREBY GRANTED TO THE UNIVERSITY OF ALBERTA LIBRARY TO REPRODUCE SINGLE COPIES OF THIS THESIS AND TO LEND OR SELL SUCH COPIES FOR PRIVATE, SCHOLARLY OR SCIENTIFIC RESEARCH PURPOSES ONLY.

THE AUTHOR RESERVES OTHER PUBLICATION RIGHTS, AND NEITHER THE THESIS NOR EXTENSIVE EXTRACTS FROM IT MAY BE PRINTED OR OTHERWISE REPRODUCED WITHOUT THE AUTHOR'S WRITTEN PERMISSION.

Yanmin Li

(Student's Signature)

Physics Department

University of Alberta

Edmonton, Alberta T6G 2J1

(Student's Permanent Address)

Date: Jan 18, 1990

UNIVERSITY OF ALBERTA

FACULTY OF GRADUATE STUDIES AND RESEARCH

THE UNDERSIGNED CERTIFY THEY HAVE READ, AND RECOMMEND TO THE FACULTY OF GRADUATE STUDIES AND RESEARCH FOR ACCEPTANCE, A THESIS ENTITLED **BEAM-LASER LIFETIME MEASUREMENTS FOR THE 3P LEVELS OF Mg II**

SUBMITTED BY **YANMIN LI**

IN PARTIAL FULFILLMENT OF THE REQUIREMENTS FOR THE DEGREE OF **MASTER OF SCIENCE**

IN PHYSICS (ASTROPHYSICS)

Dr. E. H. Pinnington (Supervisor)

Dr. R. Fedosejevs

Dr. J. A. Kernahan

Dr. M. E. Evans

Date:

FOR MY PARENTS: SHUTANG AND JUHUAN

ABSTRACT

The lifetimes of the resonance 3p levels of Mg II are accurately measured by using the beam-laser method. The accuracy for the measured lifetimes is better than 1%. Frequency-doubling optics are incorporated in the present experiment to generate UV radiation around 280 nm. The charge-integration technique is used to avoid the pile-up errors, which occur with single-photon counting. An order-of-magnitude estimate is made of the required laser power for saturation to be achieved. The success of the experiment justifies this point. The theory of frequency doubling is presented. Methods for estimating the statistical error associated with extracting the lifetime from the measured decay curve are discussed. The contributions from various possible sources of systematic error are estimated. The results of this experiment are compared with previous experimental and theoretical works. Observations of the fluorescence following two-step excitation and direct two-photon excitation are made using Doppler tuning.

ACKNOWLEDGEMENTS

I am very much grateful to my supervisor, Dr. E. H. Pinnington, for his guidance and help to complete this project successfully in the the past two years. His financial support for me being a graduate student here and participating in an international conference is also gratefully acknowledged.

Special thanks are extended to Dr. W. Ansbacher for his cooperation on the experiment and many interesting discussions. I would also like to thank Dr. J. A. Kernahan for his help in planning the graduate program.

Many thanks to Ron Gardner and Larry Coulson of the Radiation Research Laboratory are offered for teaching me the basics of TEX, the computer program used to prepare this thesis.

Finally, thanks are extended to the Department of Physics for the financial support in the past two years.

TABLE OF CONTENTS

CHAPTER I INTRODUCTION

1.1 Introduction 1

CHAPTER II AN ESTIMATION OF REQUIRED LASER POWER

2.1 Absorption and Emission 7

2.2 Saturation and Rabi Oscillation 9

2.3 Line Shape and Power Broadening due to An Intense Laser Pulse 10

2.4 An Estimation of Required Laser Power 11

CHAPTER III THEORY OF FREQUENCY DOUBLING

3.1 Introduction to Nonlinear Optical Generation 20

3.2 The Nonlinear Optical Susceptibility Tensor 21

3.3 An Anharmonic Oscillator Model 23

3.4 Coupled Wave Equations in a Nonlinear Medium 26

3.5 Phase Matching 30

3.6 Focussing 35

CHAPTER IV THE EXPERIMENTAL SETUP

4.1 Outline of The Experimental Setup 43

4.2 Laser-Frequency-Doubling Optics 49

4.3 Detection System and Charge Integration 50

CHAPTER V DATA COLLECTION AND ANALYSIS

5.1 Data Collection 55

5.2 Timing Sequence 56

5.3 Normalization 58

5.4 Fitting the Single-Exponential Decay Curve 59

5.5 Systematic Sources of Error 62

CHAPTER VI LIFETIME MEASUREMENT OF THE 3P LEVELS OF Mg II AND AN OBSERVATION OF TWO-STEP PHOTON EXCITATION

6.1 Lifetimes of the 3p Levels of Mg II 70

6.2 An Observation of the Fluorescence of Two-Step Excitation 74

CHAPTER VII CONCLUSION

7.1 Conclusion 80

Bibliography 82

Appendix Mg II Decay Data 86

LIST OF FIGURES

Fig. 1.1-1 Level diagram of Mg II. 1

Fig. 2.4-1 Schematic diagram of a two level system 16

Fig. 3.5-1 Normal (index) surfaces for the ordinary and extraordinary rays in a negative ($n_e < n_0$) uniaxial crystal. If $n_e^{2\omega} < n_0^{\omega}$, the condition $n_e^{2\omega}(\theta) = n_0^{\omega}$ is satisfied at $\theta = \theta_m$. 32

Fig. 3.5-2 The relative orientation of $\vec{E}, \vec{D}, \vec{H}, \vec{s}$ and the Poynting vector, $\vec{E} \times \vec{H}$, in an anisotropic crystal. The vectors $\vec{D}, \vec{E}, \vec{s}$, and $\vec{E} \times \vec{H}$ lie in one plane. 34

Fig. 3.6-1 Diagram of the Gaussian beam being focussed in a crystal 39

Fig. 3.6-2 The function of $F^2(u,t,q)$ as a function of u for $q = 0$ and several values of t. 41

Fig. 3.6-3 The function of G(t). 42

Fig. 4.1-1 Excitation and transition scheme of the laser experiment. 44

Fig. 4.1-2 Schematic diagram of the experiment setup. 46

Fig. 4.1-3 Target chamber. 48

Fig. 4.2-1 Angular tuning curve of KDP with Type I phase matching. 51

Fig. 4.3-1 Schematic diagram of a charge sensitive pre-amplifier. 53

Fig. 5.2-1 Timing sequence of data collection. 57

Fig. 5.5-1 Effect of the laser power drop on the decay curve. 64

Fig. 5.5-2 Effect of the dead time on the decay curve. 67

Fig. 6.1-1 A sample decay curve. A) with charge-integration and B) with photon counting. 71

Fig. 6.2-1 An observation of the fluorescence of two-step excitation. 77

Fig. 6.2-2 Diagram of a three level system. 76

LIST OF TABLES

Table 2.4-1 Atomic linewidth due to power broadening (GHz) 13

Table 5.4-1 Comparision of different fitting methods 62

Table 5.5-1 Systematic sources of error 68

Table 6.1-1 Summary of lifetime measurements for $^2P_{3/2}$ 73

Table 6.1-2 Summary of lifetime measurements for $^2P_{1/2}$ 74

Table 6.1-3 Lifetimes of the 3p levels of Mg II 75

Chapter 1 Introduction

1.1 Introduction

The accurate determination of atomic lifetimes is of much interest in laser spectroscopy, plasma physics, and astrophysics. It is central to radiative transfer calculations, which often turn out to be needed to construct the stellar interior and atmosphere models and are related directly to the observable stellar abundances [Mi87].

The resonance doublet in Mg II, ^2S–^2P, as shown in Fig. (1.1-1), is prominent in many astrophysical spectra [Fi76]. It is therefore not surprising that its oscillator strength has been the subject of many experimental [Smi66, BBB70, SL71, Lil80] and theoretical investigations [La75, Gan87, Hi88, Ti88]. A survey of the literature shows that the various theoretical approaches yielded results with a spread of 10%. Unfortunately, the precision of the various experiments so far has not been sufficient to demonstrate clearly which is the best method of calculation.

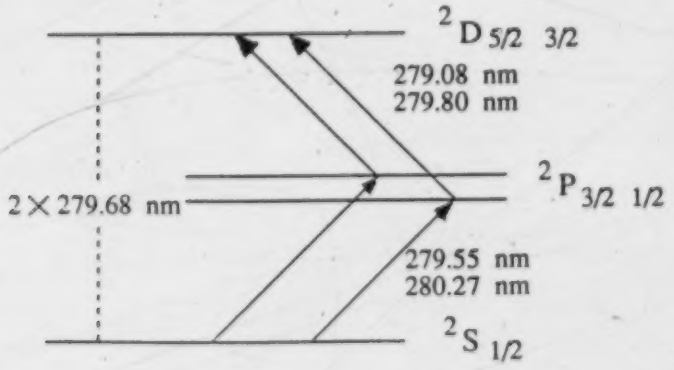

Fig. 1.1-1 Level diagram of Mg II.

In ab initio Dirac-Fock (DF) calculations, the fine structure of the 3p levels is treated in a fully relativistic manner, which is very important for high stages of ionization. However, these calculation do not adequately describe correlation effects and show a large disagreement with the experimental results. Nonrelativistic multiconfiguration Hartree-Fork calculations have been made, which include electron-correlation corrections. However, the lifetime results obtained in this manner are not truly ab initio, since only a single value for the line strength is obtained for both 3p levels, and the experimental wavelengths must be used to obtain level lifetimes. In considering the core polarization (correlation) effects, it is necessary to justify the choice of the core radius, which relies on a comparison with the observed energy levels [Tc88].

There are several ways to measure the lifetimes of the excited states of ions or neutral atoms, such as phase shift, Hanle effect, beam-foil, and so on. Of these methods, beam-foil spectroscopy [BFS] is one of the most successful and versatile techniques for atomic physics [Ma88]. It allows the study of atomic transitions and energy levels as well as the determination of atomic lifetimes.

In BFS, fast ions from an accelerator are sent through a thin solid target, usually a carbon foil, where they are ionized and excited. In principle, it can produce almost any excited state of any element in any ionization stage. One of the major advantages is that the fast moving beam provides an excellent time resolution (typically 10^{-10}s, but it can be better than 10^{-12}s in favorable cases) for lifetime measurement [Ga82]. Therefore, much work has been done in using and improving the technique since it was introduced by Kay and Bashkin in the early 1960's. The basic

principle behind this technique is that the ions or neutral species, in excited states after foil excitation, will decay into lower levels spontaneously. Direct observation of the fluorescence at various distances downstream from the foil then yields the decay curve. If only a single level is populated, then the decay curve follows a simple exponential and can be easily fitted by a least-squares method. However, since the foil excitation is non-selective, it is common that the resultant decay curve is the sum of several exponentials due to the well-known cascading effect, i.e., the levels of interest are repopulated by yet higher levels. Although the ANDC method has been used to account for the cascade contribution, the procedure is still quite delicate[TC88], setting a lower limit to the uncertainty of typically $5 - 10$ %. Moreover, it is much more difficult to tell the weights of the different lines in the fitting function when they are close in wavelength, as in the present case.

As mentioned above, BFS needs to be improved to take account of cascading. Since the advent of the laser in the early $1960's$, it has been widely used in studies of atomic spectroscopy. Instead of using a foil, a laser beam is used to excite the ion beam. By tuning the wavelength of the dye laser (pumped by an excimer or argon ion laser), a level of interest can be populated selectively. This avoids cascading and yields a single exponential decay curve. This is called the beam-laser technique. The laser excitation of fast beams has turned out to yield the most accurate lifetimes known in atomic physics up to now [Ha86]. Many papers on lifetime measurements with this method have been published with an accuracy of 1 %,or better [Ha86, GPA87, Ga82].

In beam-laser measurements we need to consider the type of laser to be used, as well as the configuration of the two beams. In principle, the continuous

wave [CW] is preferred for the visible region, since larger signal rates can be obtained with less scattered laser light. However, the much higher peak power of pulsed lasers is required to extend the measurements down to the ultraviolet wavelength, as in the case of frequency-doubling for the study of the resonance doublet of Mg II. Turning to the methods of crossing the ion and laser beams, the collinear geometry uses the laser beam parallel or anti-parallel with the ion beam and this permits a higher spectral resolution. This is important for studies of fine structure and in tests of QED. However, for the measurement of lifetimes, the two beams normally intersect at a large angle ($45° - 90°$) to provide the required time resolution. Furthermore, this permits Doppler tuning across the laser resonance to observe two-photon excitation in the present experiment.

As seen from Fig. (1.1-1), the resonance of Mg II falls in the ultraviolet region, which is beyond the present spectral range of dye lasers ($400nm - 600nm$). Fortunately, the frequency-doubling technique makes it feasible to study spectra in the UV. With a high input laser power, a nonlinear optical crystal can give second harmonic generation (SHG), *i.e.*, doubling the frequency of the incident radiation. Using a newly acquired KDP(KH_2PO_4) crystal and Rhodamine 590 dye, pulsed tunable radiation around 280 nm has been generated with a typical mean power of 1–5 mW at a repetion rate of 200 Hz.This corresponds to a peak pulse intensity at the ion beam of around 40 kW/cm^2.

Another aspect of the present experiment is that the output from the photomultiplier used to detect the fluorescence radiation was recorded using gated charge-integration, rather than the usual single-photon counting. In this way it was

possible to avoid the pile-up problems usually encountered with pulsed laser fluorescence.

Chapter 2 presents an estimation of the UV laser power needed for the saturation of ion beams. It is based on a discussion of the various line broadening mechanisms: natural linewidth, Doppler broadening, and power broadening due to the intense laser field. Calculations for two extreme cases are made to give an order of magnitude for the required laser power.

The principle of nonlinear optics is outlined in Chapter 3 in terms of a simple anharmonic oscillator model, which gives a clear indication of what the nonlinear susceptibility is about, and the semi-classical electromagnetic formulation, which allows the discussion of the nonlinear interaction of the fundamental and generated waves within the crystal, where phase matching and focussing play an important role for a high conversion efficiency of the second harmonic.

Chapter 4 describes the experimental setup used for the measurement of lifetimes using the beam-laser technique. The problems encountered in the frequency-doubling optics are also discussed. The principle of charge integration is briefly outlined.

Chapter 5 discusses the data collection system as well as the method used for analyzing the data. The timing sequence is explained in detail. The least-squares fitting method is used to extract the lifetime. An estimate is given for the various sources of error. This leads to an accuracy of better than 1%.

Chapter 6 presents the experimental lifetime results for the 3p levels of Mg II, with 3.873 ± 0.037 and 3.819 ± 0.035 ns for $^2P_{1/2}$ and $^2P_{3/2}$, respectively.

Observation of both two-step photon excitation and direct two-photon excitation is discussed.

Chapter 2 An Estimation of Required Laser Power

2.1 Absorption and Emission

Atoms or ions may be excited to higher states by absorbing photons. These excited species will decay back to the lower states, emitting radiation in all directions. It is useful to employ the Einstein theory to treat these phenomena when dealing with an ordinary light source where the intensity is quite low, so that the spontaneous emission is dominant. It follows that the intensity of the light beam falls off exponentially as it goes through the system of atoms or ions. For low intensities, the atoms or ions absorb radiation at a rate proportional to the intensity. This is true for all ordinary broad-band illumination.

There are three competing processes occurring simultaneously in the excitation. Each of them is governed respectively by one of the three intrinsic coefficients: spontaneous emission coefficient A_{21}, absorption coefficient B_{12}, and stimulated emission coefficient B_{21}. These are related by the Einstein relations. In order to excite a large number of ions, one has to increase the intensity of the excitation source. As the intensity of the incident radiation is increased, the stimulated emission probability increases and eventually becomes dominant over spontaneous emission since it is proportional to the product of the density of the incident radiation and the stimulated coefficient B_{21}. Generally speaking, it is difficult to calculate how much power is needed to excite as large a fraction of the ion beam as possible. However, we can make some order of magnitude estimates.

A lower limit for the required power may be estimated from the assumption that the transition probability for absorption should be at least equal to

the spontaneous transition probability,

$$\rho B_{12} = A_{21} \qquad (2.1-1)$$

where ρ is the radiation energy density per unit frequency range. Recalling that [Lo83]

$$\frac{\hbar\omega^3}{\pi^2 c^3} B_{21} = A_{21} \qquad (2.1-2)$$

and assuming that the statistical weights of the levels are equal, upon comparing Eqns.(2.1-1) and (2.1-2), we obtain

$$\rho = \frac{\hbar\omega^3}{\pi^2 c^3} \qquad (2.1-3)$$

For $\lambda = 280nm$,

$$\rho = 1.21 \times 10^{-13} \frac{Js}{m^3} \qquad (2.1-4)$$

Thus, the intensity per unit frequency range is

$$I = \rho c = 3.62 \times 10^{-5} \frac{Ws}{m^2} \qquad (2.1-5)$$

For a laser pulse with a width of 11.5 GHz (0.003 nm at 280 nm), the intensity is

$$I_{pulse} = I \times 11.5GHz = 0.042kW/cm^2 \qquad (2.1-5)$$

This estimate is certainly much too low since we actually require absorption to dominate spontaneous emission if we are to excite a large fraction of the radiated ions. However, when absorption becomes important, it is inevitable that stimulated emission will also become important. This simple low intensity picture is therefore difficult to extend to the high intensity situation. We will therefore now examine the question from the high intensity point of view.

2.2 Saturation and Rabi Oscillation

When the intensity of the incident electromagnetic radiation is raised so high that absorption and stimulated emission are dominant over spontaneous emission, the system becomes saturated. At saturation, the populations in the upper and lower levels are determined by the statistical weights, g_2 and g_1, as follows

$$\frac{N_2}{N_1} = \frac{g_2}{g_1} \qquad (2.2-1)$$

where N_2, N_1 are the number of ions in the upper and lower levels respectively. Once saturation is reached, there is no point in increasing power further from the point of view of the number of the excited ions.

There is a second way to approach this problem which is via the density matrix method. As will be indicated in the following sections, the phenomenon of Rabi oscillation and power broadening follow naturally from this theory. A second estimation of the laser power needed to excite the ion beam is based on these considerations.

Using the rotating-wave approximation and neglecting radiation damping, it can be shown that the solution to the simultaneous equations for the elements of the atomic density matrix has an oscillatory behaviour in terms of the Rabi frequency [Lo83],

$$\{(\omega_0 - \omega)^2 + |V|^2\}^{\frac{1}{2}} \qquad (2.2-2)$$

where ω_0 is the frequency of atomic transition,

ω is the frequency of incident radiation

$|V| = E_0 X_{12}/\hbar$

$X_{12} = \int \psi_1 ex \psi_2 d^3r$ x-component of electric dipole moment

ψ_1 and ψ_2 are the eigenvectors for the states 1 and 2 respectively

The population in the upper state will change according to the Rabi frequency. However, the oscillations of the populations in the excited states will be damped out because of the action of radiative damping. Finally, an equilibrium of populations among the states can be reached. In other words, saturation can be achieved.

2.3 Line Shape and Power Broadening due to An Intense Laser Pulse

In general, the absorption properties of ions depend on the line profile. In addition to the natural width, Doppler broadening due to the thermal velocity of ions and collision broadening also contribute to the absorption line shape. In the present experiment, the ion density in the beam is so low that collisional effects can be ignored. More specifically, the beam divergence after passing the resolving magnet and thermal velocities originating from the ion source, combined in cross-beam geometry, constitute the major sources of line broadening.

As indicated earlier, an atom in an intense laser field forms a strongly coupled unit and is quite different from an atom exposed to a weak field, where the interaction takes place between independent identities. It is worth noting this difference. The strong interaction produces an energy level shift as well as the change of the atomic lineshape. It is shown [Lo83] from the density-matrix method that a susceptibility is produced as

$$\chi(\omega) = \frac{Ne^2|D_{12}|^2}{3\epsilon_0 \hbar v} \frac{\omega_0 - \omega + i\gamma}{(\omega_0 - \omega)^2 + \gamma^2 + \frac{1}{2}|V|^2} \qquad (2.3-1)$$

where $|D_{12}|$ is the dipole moment of ion

v is the volume

N is the number of ions within volume v

γ is the damping constant, i. e, half natural line width

| V | is the same as before, relating to the field strength.

This is no longer a linear susceptibility because the field strength E_0 is contained in the quantity $|V|$. The overall shape is similar to the natural line profile except for the additional contribution $\frac{1}{2}|V|^2$ in the denominator.

Therefore, the linewidth of the atomic transition is increased from 2γ to

$$2(\gamma^2 + \frac{1}{2}|V|^2)^{\frac{1}{2}} \qquad (2.3-2)$$

This additional contribution to the linewidth is known as power broadening or saturation broadening.

2.4 An Estimation of Required Laser Power

Besides power broadening and Doppler broadening, the laser linewidth itself is the third important factor in the excitation. It is determined by the cavity where amplification occurs. In a Fabry-Perot type of cavity, the free spectral range and finesse give the minimum width. Using a grating for wavelength-selection, the width depends on the resolving power, which is the product of the total number of grooves illuminated and the order used. One can illuminate a different number of grating grooves and use different orders to obtain a constant width over the region of interest. For the dye laser used here, the grazing-incidence geometry is used, so that a very narrow linewidth can be achieved.

For the sake of simplicity of calculation, we assume that the width of laser radiation is constant over the spectral range of interest (200 nm –300 nm)at around 0.003 nm. It can be represented in the frequency domain as follows

$$\Delta\nu_L = \frac{\nu}{\lambda}\Delta\lambda = \frac{c}{\lambda^2}\Delta\lambda \qquad (2.4-1)$$

For radiation in the ultraviolet region, frequency uncertainties fall between

$$\Delta\nu_L = 10GHz \qquad for\ \ 300nm;$$
$$\Delta\nu_L = 22.5GHz \qquad for\ \ 200nm \qquad (2.4-2)$$

We have a two-level system with the upper and lower levels denoted by 2 and 1 respectively. As shown in Eqn. (2.3-2), the atomic linewidth due to power broadening can be expressed as [Go88]

$$\Delta\omega_P = \tau^{-1}\sqrt{1+(2W_R)^2\tau^2} \qquad (2.4-3)$$

where τ is the lifetime of the upper level 2

$W_R^2 = I\frac{A_{21}}{\omega_0^3}\frac{g_2}{g_1}\left(\frac{12\pi c^2}{\hbar}\right)$

ω_0 is the line center frequency

I is the laser input intensity

g_i's are the statistical weights of the levels

Usually the second term under the square root is dominant; as such, Eqn. (2.4-3) becomes

$$\Delta\omega_P = \sqrt{2}W_R$$
$$= \sqrt{2}\left(\frac{IA_{21}}{\omega_0^2}\frac{g_2}{g_1}\right)^{1/2}\left(\frac{12\pi c^2}{\hbar}\right)^{1/2} \qquad (2.4-4)$$

In terms of frequency,

$$\Delta\nu_P = \frac{3.1\times10^{12}}{2\pi}\sqrt{IA_{21}\lambda^3 g_2/g_1} \qquad (2.4-5)$$

Table. 2.4–1 Atomic linewidth due to power broadening (GHz)

$\lambda(nm)$	800	600	500	400	350	300	270	250	220	200	
I=1	4.0	2.6	1.9	1.4	1.1	0.92	0.79	0.70	0.58	0.50	a)
$\frac{MW}{m^2}$	6.4	4.2	3.2	2.3	1.8	1.5	1.2	1.1	0.92	0.80	b)
		7.3	5.5	3.9	3.2	2.6	2.2	1.9	1.6	1.4	c)
5	9.0	5.8	4.4	3.2	2.6	2.1	1.8	1.6	1.3	1.1	
		9.3	7.1	5.1	4.1	3.3	2.8	2.5	2.1	1.8	
				8.8	7.2	5.7	4.9	4.4	3.6	3.1	
10	12.7	8.3	6.3	4.5	3.7	2.9	2.5	2.2	1.8	1.6	
		13.2	10.0	7.2	5.8	4.6	4.0	3.5	2.9	2.5	
					10.2	8.1	6.9	6.2	5.1	4.4	
50	28.4	18.5	14.1	10.0	8.2	6.5	5.6	5.0	4.1	3.5	
					13.1	10.4	8.9	7.9	6.5	5.7	
						18.0	15.5	13.7	11.4	9.8	
100	40.2	26.1	19.8	14.2	11.6	9.2	7.9	7.0	5.8	5.0	
					18.6	14.7	12.6	11.2	9.2	8.0	
						25.6	21.8	19.5	16.1	13.9	

(a For A=$0.13\times10^9 s$ ($\tau = 7ns$)

(b A=$0.33\times10^9 s$ ($\tau = 3ns$)

(c A=$1\times10^9 s$ ($\tau = 1ns$)

Some typical values are worked out and shown on Table.(2.4–1). It shows that the width varies from 1 to several tens of GHz for the spectral range of 800 nm to 200 nm and lifetimes over 1 to 7 ns with the radiation of intensity from 1 to 100 MW/m^2.

As mentioned earlier, the Doppler broadening is due to the velocity spread of ions in the beam, which is around 0.5%. Taking the typical parameters,

$$v = 1mm/ns = 1 \times 10^6 m/s \qquad (2.4-6)$$

we have

$$\Delta v = 5 \times 10^3 m/s \qquad (2.4-7)$$

The spread in frequency is

$$\Delta\nu' = \frac{\Delta v}{\lambda} cos\theta \qquad (2.4-8)$$

where θ is the angle between the ion and laser beams.

For $\lambda = 300$ nm, $\Delta\nu' = 11.8$ GHz (2.4-9)

$\lambda = 200$ nm, $\Delta\nu' = 17.7$ GHz (2.4-10)

Now we are in a position to make a comparison among three sources of line broadening which characterize the interaction picture. In summary, we have

$\Delta\nu_L$ —width of laser line

$\Delta\nu_P$ —width due to power broadening

$\Delta\nu'$ —width due to the velocity spread.

From Eqns. (2.4–2) and (2.4–9, 10), the width of the laser line is of the same order of magnitude as the Doppler effect, which simplifies the problem. What

is left to be done is to compare the broadening due to laser power, $\Delta\nu_P$. First we consider the contribution due to the laser linewidth, $\Delta\nu_L$.

In general, we have to integrate over the frequency domain to account for the contribution of the lineshape. For simplicity, we consider two extreme cases. One is that $\Delta\nu_P \gg \Delta\nu_L$, and the other is $\Delta\nu_P \ll \Delta\nu_L$. If the two are comparable, the result should be somewhere in between.

Before we make any calculation, let us clarify our system and the assumptions to be used.

— a two-level system is assumed

— the laser intensity is strong enough to excite the ion beam to the saturation state within a period of time much less than the radiative lifetime. We will take this period, τ_{exc}, to be $4 \times 10^{-10} s$

— statistical weights for the upper and lower states, g_m and g_n, are assumed equal

— for simplicity, all lineshapes are assumed to be rectangular with

$$g(\nu) = \frac{1}{\Delta\nu} \qquad (2.4-11)$$

— at saturation

$$\left.\begin{aligned} &\frac{N_m}{g_m} = \frac{N_n}{g_n} \\ &if \quad g_m = g_n \\ &N_m = N_n = \frac{1}{2}N_0 \end{aligned}\right\} \qquad (2.4-12)$$

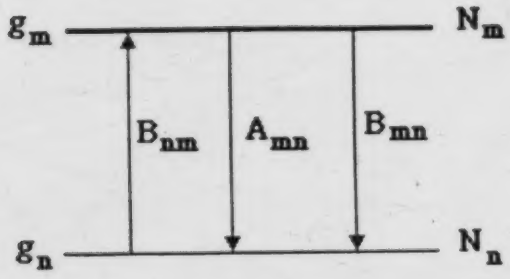

Fig. 2.4-1 Schematic diagram of a two level system

where N_0 is the total ion density

$N_{m,n}$ are the numbers of ions per unit volume in the upper and lower levels respectively.

Having made the above simplifications, we calculate the two cases.

a) $\Delta\nu_L \gg \Delta\nu_P$

In this case, $\Delta\nu_L$ is important. Thus, we have

$$\tau_{exc} N_0 B_{nm} [\rho g_L(\nu)] = N_m \qquad (2.4-13)$$

but I=ρ c,

therefore,

$$I = c\frac{N_m}{N_0}\frac{1}{\tau_{exc} B_{mn} g_L(\nu)} \qquad (2.4-14)$$

Using $g_m B_{mn} = g_n B_{nm}$ and Eqn.(2.4-12),

$$I = c\frac{1}{2}\frac{1}{\tau_{exc}}\frac{1}{B_{mn}g_L(\nu)}$$
$$= \frac{1}{c}\frac{1}{2}\frac{1}{\tau_{exc}}\frac{8\pi h}{\lambda^3}\frac{1}{A_{mn}\frac{1}{g_L(\nu)}} \qquad (2.4-15)$$

Recall $\frac{1}{g_L(\nu)} = \Delta\nu_L = \frac{c}{\lambda^2}\Delta\lambda$,

$$I = \frac{c^2}{2\tau_{exc}}\frac{8\pi h}{\lambda^5}\frac{1}{A_{mn}}\Delta\lambda \qquad (2.4-16)$$

We now consider some specific examples.

Example 1, with λ=300nm, τ_{exc}=$4 \times 10^{-10} s$

A_{mn}=$0.2 \times 10^9\ s^{-1}$

$\frac{1}{g_L(\nu)} = 11.8\times 10^9 s^{-1}$

I = 11.6 MW/m^2 = 1.2 kW/cm^2 (2.4 - 17)

Example 2 with λ = 200nm, $\tau_{exc} = 3 \times 10^{-10}$ s

$A_{mn} = 0.3 \times 10^9 s^{-1}$, $\frac{1}{g_L(\nu)} = 17.7\times 10^9$ Hz

I = 78 MW/m^2=7.8kW/cm^2 (2.4 - 22)

b) $\Delta\nu_P \gg \Delta\nu_L$

The laser radiation is considered as monochromatic radiation.

$$\tau_{exc} N_0 (B_{nm}\ g_{atomic})\rho = N_m \qquad (2.4-19)$$

but I = ρ c,

$$I = c\frac{1}{2}\frac{1}{\tau_{exc}}\frac{1}{B_{mn}}\frac{1}{g_{atomic}}$$
$$= c\frac{1}{2}\frac{1}{\tau_{exc}}\frac{8\pi h}{\lambda^3}\frac{1}{A_{mn}}\Delta\nu_P \qquad (2.4-20)$$

From Eqn. (2.4-5),

$$I = (\frac{c}{\tau_{exc}} 2h \times 3.1 \times 10^{12})^2 \frac{1}{\lambda^3 A_{mn}} \frac{g_m}{g_n} \qquad (2.4-21)$$

Example 3,

$$\tau_{exc} = 4 \times 10^{-10} s$$

$$\lambda = 300nm$$

$$A_{mn} = 0.2 \times 10^9 s^{-1}$$

$$g_m = g_n$$

$$\text{I} = 1.8 \text{ MW } /m^2 = 0.18 kW/cm^2 \qquad (2.4 - 22)$$

Example 4

$$\tau_{exc} = 3 \times 10^{-10} s$$

$$\lambda = 200nm$$

$$A_{mn} = 0.3 \times 10^9 s^{-1}$$

$$\text{I} = 5.3 \text{ MW } /m^2 = 0.53 kW/cm^2 \qquad (2.4 - 23)$$

Now let us turn to the laser power for the present experiment. The typical parameters are as follows

Pulse duration	$5 \times 10^{-9} s$
Repetition rate	200/s
Mean power	5 mw
Cross-section of laser beam	$0.7 \times 0.2 = 0.14 cm^2$

Therefore,

$$\text{Peak Power } = \frac{5 \times 10^{-3}/0.14}{200 \times 5 \times 10^{-9}} = 35.7 kW/cm^2 \qquad (2.4-24)$$

It can be seen from Eqn. (2.4-17, 18, 22, 23, 24) that we have enough power to saturate the ion beam. As will be discussed in Chapter 6, a mean power of 2mW UV at 280 nm is sufficient to give a useful signal without introducing an excessive amount of scattered laser light.

Chapter 3 Theory of Frequency Doubling

3.1 Introduction to Nonlinear Optical Generation

In order to produce coherent ultraviolet radiation, it is necessary to make use of the second harmonic generation (SHG) of the dye laser output since there exists no continuous tuning laser source available up to now in this region. Shortly after the demonstration of the laser, Franken et al [Fr61] generated the second harmonic of a Ruby laser in a quartz crystal. The success of this experiment relied directly on the enormous increase of power spectral brightness provided by the laser source compared to incoherent sources. Power densities greater than $10^9 W/cm^2$ became available; these correspond to an electric field strength of $10^6 V/cm$.This field strength is comparable to the field strength within the atom, and therefore it is not surprising that materials respond in a nonlinear manner to the applied field.

Second harmonic generation is a process which occurs when there is a polarization proportional to the square of the field. Harmonic generation in the optical region is similar to the more familiar harmonic generation at radio frequencies, with one important exception. In the radio-frequency range, the wavelength is usually much larger than the harmonic generator, so that the interaction is localized in a volume much smaller than the dimensions of a wavelength. In the optical region the situation is usually reversed and the nonlinear medium extends over many wavelengths. This leads to the consideration of propagation effects since the electromagnetic wave interacts over an extended distance with the generated nonlinear polarization. If this interaction is to be efficient, the phases of the propagating wave

and the generated polarization must be coherent. This is referred to as phase matching in nonlinear optics. For second harmonic generation, phase matching implies that the phase velocities of the fundamental and second harmonic waves are equal in the nonlinear material. Since optical materials are dispersive, it is not possible to achieve equal phase velocities in isotropic materials. However, phase velocity matching can be achieved in birefringent crystals by using birefringence to offset the dispersion.

In the following sections, we begin with a discussion of nonlinear polarization in a classical model, which will give a very simple idea of what the nonlinear response is about. The electromagnetic formulation will then be presented dealing with the coupled wave equations for fundamental and generated waves. As a consequence, conversion efficiency, phase matching schemes and focussing follow.

3.2 The Nonlinear Optical Susceptibility Tensor

When a medium is subjected to an electrical field the electrons in it are polarized. For a weak electrical field, the polarization is linearly proportional to the applied field

$$\vec{P} = \epsilon_0 \chi^{(1)} \vec{E} \qquad (3.2-1)$$

where $\chi^{(1)}$ is the linear optical susceptibility and ϵ_0 is the permittivity of free space with the value of $8.85 \times 10^{-12} F/m$ in SI units. The linear susceptibility is related to the medium's index of refraction n by $\chi^{(1)} = n^2 - 1$.

In a crystalline medium the linear susceptibility is a tensor that obeys the symmetry properties of the crystal. Thus, for isotropic media there is only one value of the index; for uniaxial crystals two values, n_0 the ordinary and n_e the extraordinary indices of refraction; and for biaxial crystals three values $n_\alpha, n_\beta, n_\gamma$

A linear polarization is an approximation to the complete constitutive relation which can be written as an expansion in powers of the applied field

$$\vec{P} = \epsilon_0(\chi^{(1)} + \chi^{(2)}\vec{E} + \chi^{(3)}\vec{E}^2 + \ldots)\vec{E} \qquad (3.2-2)$$

where $\chi^{(2)}$ is the second order nonlinear susceptibility and $\chi^{(3)}$ is the third order nonlinear susceptibility , and so on. $\chi^{(2)}$ gives rise to second harmonic generation among other processes.

Like the linear susceptibility, the second-order susceptibility must display the symmetry properties of the crystal medium. An immediate consequence of this fact is that the second order nonlinear coefficients must vanish in a crystal with a center of symmetry. Nonlinear optical effects are therefore restricted to acentric materials.

The tensor properties of $\chi^{(2)}$ can be displayed by writing the nonlinear polarization in the form

$$P_i(t) = \epsilon_0 \sum_{jk} \chi^{(2)}_{ijk} E_j(t) E_k(t) \qquad (3.2-3)$$

where $\chi^{(2)}$ is the nonlinear susceptibility tensor coupling the instantaneous fields.

It is customary to define the nonlinear susceptibility tensor in terms of the Fourier components of the fields. We define the field component at frequency ω by the Fourier relation

$$U(t) = \frac{1}{2}[U(\omega)e^{i(\vec{k}\cdot\vec{r}-\omega t)} + C.C.] \qquad (3.2-4)$$

where $C.C.$ is a complex conjugate. Substituting for the fields and polarizations in Eqn (3.2-3) we find

$$P_i(-\omega_3) = \epsilon_0 \sum_{jk} \frac{1}{2} \chi^{(2)}_{ijk}(-\omega_3, \omega_2, \omega_1) E_j(\omega_2) E_k(\omega_1)$$

$$\times exp i[(\vec{k}_2 + \vec{k}_1 - \vec{k}_3) \cdot \vec{r}] \qquad (3.2-5)$$

where we have assumed $\omega_3 = \omega_2 + \omega_1$.

In addition to crystal symmetry restrictions, $\chi^{(2)}_{ijk}$ satisfies two additional symmetry relations. The first is an intrinsic symmetry relation which can be derived for a lossless medium from general energy considerations. This relation states that $\chi^{(2)}_{ijk}(-\omega_3, \omega_2, \omega_1)$ is invariant under any permutation of the three pairs of indices $(-\omega_3, i)$; (ω_2, j); (ω_1, k) . The second symmetry relation is based on a conjecture by Kleinman [Kl62] that in a lossless medium the permutation of the frequencies is irrelevant and therefore $\chi^{(2)}_{ijk}$ is symmetric under any permutation of its indices.

It is customary to write the driving polarization for SHG in terms of a nonlinear tensor **d** defined by

$$P_i(-\omega_3) = \epsilon_0 \sum_{jk} d^{(2)}_{ijk}(-\omega_3, \omega_2, \omega_1) E_j(\omega_2) E_k(\omega_1)$$

$$\times exp i[(\vec{k}_2 + \vec{k}_1 - \vec{k}_3) \cdot \vec{r}] \qquad (3.2-6)$$

where $\omega_3 = 2\omega_1$. Comparision of Eqn.(3.2-5) with the above definition of d_{ijk} shows that

$$\chi^{(2)}_{ijk}(-\omega_3, \omega_2, \omega_1) = 2 d_{ijk}(-\omega_3, \omega_2, \omega_1) \qquad (3.2-7)$$

3.3 An Anharmonic Oscillator Model

The linear and nonlinear susceptibilities characterize the optical properties of a medium. Physically, they are related to the microscopic structure of the

medium and can be properly evaluated only with a full quantum-mechanical calculation. Here a simple model, the anharmonic oscillator , is considered to illustrate the origin of optical nonlinearity.

The model assumes that the electronic response to a driving electric field can be simulated by that of an electron in an anharmonic potential well. The equation of motion for the electron is then

$$\ddot{x} + \Gamma\dot{x} + \omega_0^2 x + ax^2 = F \qquad (3.3-1)$$

where x is the deviation from the potential minimum, ax^2 is the anharmonic restoring force, F is the driving field, and Γ is the damping constant.

We consider here the response of the oscillator to an applied field with Fourier components at frequences $\pm\omega_1$, $\pm\omega_2$:

$$F = \frac{q}{m}[E_1(e^{-i\omega_1 t} + e^{i\omega_1 t}) + E_2(e^{-i\omega_2 t} + e^{i\omega_2 t})] \qquad (3.3-2)$$

The anharmonic term ax^2 in Eqn.(3.3–1) is assumed to be small so that it can be treated as a perturbation in the successive approximation of finding a solution:

$$x = x^{(1)} + x^{(2)} + x^{(3)} + \ldots \qquad (3.3-3)$$

The induced electric polarization is simply

$$P = Nqx \qquad (3.3-4)$$

Putting Eqns.(3.3–3) and (3.3–2) back into (3.3–1) and linearizing the equation yields the first order solution:

$$x^{(1)} = x^{(1)}(\omega_1) + x^{(1)}(\omega_2) + C.C. \qquad (3.3-5)$$

$$x^{(1)}(\omega_i) = \frac{(q/m)E_i}{(\omega_0^2 - \omega_i^2 - i\omega_i\Gamma)} e^{-i\omega_i t} \qquad (3.3-6)$$

The second-order solution is obtained from Eqn.(3.3–1) by using an approximation of (3.3–5,6):

$$x^{(2)} = x^{(2)}(\omega_1 + \omega_2) + x^{(2)}(\omega_1 - \omega_2) + x^{(2)}(2\omega_1) + x^{(2)}(2\omega_2) + x^{(2)}(0) + C.C. \qquad (3.3-7)$$

$$x^{(2)}(\omega_1 \pm \omega_2) = \frac{-2a(q/m)^2 E_1 E_2}{(\omega_0^2 - \omega_1^2 - i\omega_1\Gamma)(\omega_0^2 - \omega_2^2 \mp i\omega_2\Gamma)} \times \frac{1}{(\omega_0^2 - (\omega_1 \pm \omega_2)^2 - i(\omega_1 \pm \omega_2)\Gamma)} e^{-i(\omega_1 \pm \omega_2)t} \qquad (3.3-8)$$

$$x^{(2)}(2\omega_i) = \frac{-a(q/m)^2 E_i^2}{(\omega_0^2 - \omega_i^2 - i\omega_i\Gamma)^2(\omega_0^2 - 4\omega_i^2 - i2\omega_i\Gamma)} e^{-i\omega_i t} \qquad (3.3-9)$$

$$x^{(2)}(0) = -a\left(\frac{q}{m}\right)^2 \frac{1}{\omega_0^2} \times \left(\frac{1}{(\omega_0^2 - \omega_1^2 - i\omega_1\Gamma)} + \frac{1}{(\omega_0^2 - \omega_2^2 - i\omega_2\Gamma)}\right) \qquad (3.3-10)$$

By successive iteration, higher-order solutions can also be obtained . As seen in the second-order case, new frequency components of the polarization at $\omega_1 \pm \omega_2$, $2\omega_1$, $2\omega_2$, and 0 have appeared through quadratic interaction of the field with the oscillator via the anharmonic term. The oscillating polarization components will radiate and generate new waves at $\omega_1 \pm \omega_2$, $2\omega_1$, $2\omega_2$. Thus, sum- and difference-frequency generation and second harmonic generation are readily explained. All of the above processes take place simultaneously in the nonlinear medium. One question that naturally occurs is how one process is singled out to proceed efficiently relative to the competing processes. In fact, phase matching selects the process of interest to the exclusion of the other possible processes.

3.4 Coupled Wave Equations in a Nonlinear Medium

We are now in a position to derive a set of coupled wave equations for the electromagnetic fields generated by the nonlinear driving polarization.

Our starting point is, of course, Maxwell's equations. In SI units,

$$\nabla \times \vec{E} = -\frac{\partial \vec{B}}{\partial t} \qquad (3.4-1a)$$

$$\nabla \times \vec{H} = \frac{\partial \vec{D}}{\partial t} + \vec{J} \qquad (3.4-1b)$$

with the constitutive relations

$$\begin{aligned} \vec{D} &= \epsilon_0 \vec{E} + \vec{P} \\ \vec{J} &= \sigma \vec{E} \\ \vec{B} &= \mu_0 \vec{H} \end{aligned} \qquad (3.4-2)$$

Taking the curl of Eqn. (3.4-1a) and assuming a nonmagnetic medium we have

$$\begin{aligned} \nabla \times (\nabla \times \vec{E}) &= -\frac{\partial}{\partial t}(\nabla \times \vec{B}) \\ &= -\mu_0 \frac{\partial}{\partial t}(\nabla \times \vec{H}) \\ &= -\mu_0 \frac{\partial}{\partial t}(\frac{\partial \vec{D}}{\partial t} + \vec{J}) \end{aligned}$$

rewriting the left-hand side and noting that $\nabla \cdot \vec{E} = 0$ we find

$$\nabla \times (\nabla \times \vec{E}) = \nabla(\nabla \cdot \vec{E}) - \nabla^2 \vec{E} = -\mu_0 \frac{\partial}{\partial t}(\frac{\partial \vec{D}}{\partial t} + \vec{J})$$

or

$$\nabla^2 \vec{E} - \mu_0 \sigma \frac{\partial \vec{E}}{\partial t} - \mu_0 \epsilon_0 \frac{\partial^2 \vec{E}}{\partial t^2} = \mu_0 \frac{\partial^2 \vec{P}}{\partial t^2} \qquad (3.4-3)$$

This wave equation describes the electric field in the medium, generated by the driving polarization $\vec{P}$. The equation is general and applies to all processes that

can be described in terms of a polarization. Of course, nonlinear optical interactions are included.

The fields in Eqn.(3.4–3) are the instantaneous fields. As described above, it is customary to define the nonlinear susceptibility not in terms of instantaneous fields but by their Fourier components defined by

$$\vec{E}(\vec{r},t) = \frac{1}{2}[\vec{E}(\vec{r},\omega)\exp i(\vec{k}\cdot\vec{r}-\omega t) + C.C.] \qquad (3.4-4)$$

and

$$\vec{P}(\vec{r},t) = \frac{1}{2}[\vec{P}(\vec{r},\omega)\exp i(\vec{k}\cdot\vec{r}-\omega t) + C.C.] \qquad (3.4-5)$$

We now assume propagation in the z–direction (not related to any crystal axis) to reduce Eqn.(3.4–3) to a one-dimensional equation. Substituting Eqn.(3.4–4,5) for the electric field and polarization into Eqn.(3.4-3), we find upon differentiation that

$$\frac{1}{2}\frac{\partial^2 E}{\partial z^2} + ik\frac{\partial E}{\partial z} - \frac{\mu_0\sigma}{2}\frac{\partial E}{\partial t} + \frac{i\omega\mu_0\sigma}{2}E - \frac{\mu_0\epsilon_0}{2}\frac{\partial^2 E}{\partial t^2} + i\omega\mu_0\epsilon_0\frac{\partial E}{\partial t}$$
$$= \frac{\mu_0}{2}\frac{\partial^2 P}{\partial t^2} - i\omega\mu_0\frac{\partial P}{\partial t} - \frac{i\omega^2\mu_0}{2}P \qquad (3.4-6)$$

In the slowly-varying-amplititude approximation,

$$\omega^2 P \gg \omega\frac{\partial P}{\partial t} \gg \frac{\partial^2 P}{\partial t^2}$$

and

$$k\frac{\partial E}{\partial z} \gg \frac{\partial^2 E}{\partial z^2} \qquad (3.4-7)$$

$$\omega E \gg \frac{\partial E}{\partial t}$$

With these approximations the wave equation reduces to

$$ik\frac{\partial E}{\partial z} + \frac{i\omega\mu_0\sigma}{2}E = -\frac{i\omega^2\mu_0}{2}P \qquad (3.4-8)$$

Dividing by ik and noting that $k = n\frac{\omega}{c}$, we find that

$$\frac{\partial E}{\partial z} + \alpha E = \frac{i\mu_0 c\omega}{2n}P \qquad (3.4-9)$$

where $\alpha = \mu_0\sigma c/2n$ is the electric-field loss coefficient. The equation relates the envelopes of the electric field and driving polarization.

Having obtained the Eqn.(3.4–9), we are now in a position to apply it to the second harmonic generation. In writing the nonlinear polarization in Eqn.(3.4–4,5) we include the frequency and spatial properties of the field. For second harmonic generation with $\omega_3 = 2\omega$ and $\omega_1 = \omega_2 = \omega$ the polarization reduces to

$$P(2\omega) = \epsilon_0 d_{eff} E(\omega)E(\omega)exp[i(2\vec{k}_\omega - \vec{k}_{2\omega})\cdot\vec{r}] \qquad (3.4-10)$$

and

$$P(\omega) = 2\epsilon_0 d_{eff} E(2\omega)E^*(\omega)exp[i(2\vec{k}_{2\omega} - 2\vec{k}_\omega)\cdot\vec{r}] \qquad (3.4-11)$$

where d_{eff} is the effective nonlinear coefficient for the interaction dependent on crystal symmetric and propagation direction relative to the crystal axis in the medium.

Substituting the driving polarization $P(2\omega)$ and $P(\omega)$ into Eqn.(3.4-9) we find

$$\frac{dE(\omega)}{dz} + \alpha_\omega E(\omega) = i\kappa E(2\omega)E^*(\omega)e^{i\Delta kz} \qquad (3.4-12)$$

$$\frac{dE(2\omega)}{dz} + \alpha_{2\omega} E(2\omega) = i\kappa E(\omega)E(\omega)e^{-i\Delta kz} \qquad (3.4-13)$$

where $\Delta\vec{k} = \vec{k}_{2\omega} - 2\vec{k}_\omega$ and $\kappa = \omega d_{eff}/nc$.

The above equations can be solved by integration. However, assuming some conditions will do no harm to the general implications of the solution . Usually, the conversion efficiency is quite low; therefore, the fundamental wave is constant with distance. Thus, in a lossless medium, $\alpha = 0$, we set $dE(\omega) = 0$ and integrate Eqn.(3.4–13)

$$\int_0^{E(z=l)} dE(2\omega) = \int_{\frac{-l}{2}}^{\frac{l}{2}} i\kappa E^2(\omega) exp(-i\Delta k z)\, dz \qquad (3.4-14)$$

which gives

$$\begin{aligned} E(2\omega)|_{z=l} &= i\kappa E^2(\omega)\frac{exp(i\Delta kl/2) - exp(-i\Delta kl)}{i\Delta k} \\ &= \kappa E^2(\omega) l \frac{\sin(\frac{\Delta kl}{2})}{(\frac{\Delta kl}{2})} \end{aligned} \qquad (3.4-15)$$

In terms of intensity

$$I = \frac{nc\epsilon_0}{2}|E|^2 \qquad (3.4-16)$$

Thus,

$$\frac{I(2\omega)}{I(\omega)} = \Gamma^2 l^2 \left(\frac{\sin(\frac{\Delta kl}{2})}{(\frac{\Delta kl}{2})}\right)^2 \qquad (3.4-17)$$

where

$$\Gamma^2 l^2 = \kappa^2 |E(\omega)|^2 l^2 = \frac{2\omega^2 |d_{eff}|^2 l^2 I(\omega)}{n^3 c^3 \epsilon_0} \qquad (3.4-18)$$

This example shows that phase matching, Δk, enters into the nonlinear conversion process through the phase synchronism factor $\sin(\frac{\Delta kl}{2})/(\frac{\Delta kl}{2})$ which is unity at $\Delta kl = 0$. Also, the second harmonic conversion efficiency is proportional to $|d|^2$ and l^2, as expected, and varies as the fundamental intensity.

3.5 Phase Matching

According to Eqn.(3.4-17) a prerequisite for efficient second-harmonic generation is that $\Delta k = 0$, that is ,

$$k_{2\omega} = 2k_{\omega} \tag{3.5-1}$$

If $\Delta k \neq 0$, the second-harmonic wave generated at z_1 and propagated to z_2 is not in phase with the second harmonic wave generated at z_2. This results in the interference described by the factor

$$\frac{\sin(\frac{\Delta kl}{2})}{(\frac{\Delta kl}{2})}$$

in Eqn.(3.4-17). Two adjacent peaks of this spatial interference pattern are separated by the so-called "coherence length,"

$$l_c = \frac{2\pi}{\Delta k} = \frac{2\pi}{k_{2\omega} - 2k_{\omega}} \tag{3.5-2}$$

The coherence length l_c is thus a measure of the maximum crystal length that is useful in producing the second-harmonic power. Under ordinary circumstances it may be no larger than $10^{-2} cm$. This is because the index of refraction n_{ω} normally increases with ω, so Δk is given by

$$\Delta k = k_{2\omega} - 2k_{\omega} = \frac{2\omega}{c}(n_{2\omega} - n_{\omega}) \tag{3.5-3}$$

Thus the coherence length is

$$l_c = \frac{\lambda}{2(n_{2\omega} - n_{\omega})} \tag{3.5-4}$$

It is seen from here that the indices of refraction at the fundamental and second-harmonic frequencies must be equal in order to obtain a maximum interaction length,

$$n_{2\omega} = n_{\omega} \tag{3.5-5}$$

The technique that is used widely to satisfy the phase-matching requirement takes advantage of the natural birefringence of anisotropic crystals. In normally dispersive materials the index of the ordinary wave or the extraordinary wave along a given direction increases with frequency. This makes it impossible to satisfy (3.5-5) when both the ω and 2ω beams are of the same type, that is, when both are extraordinary or ordinary. We can, however, under certain circumstances, satisfy (3.5-5) by using two waves of different type - one ordinary and one extraordinary. To illustrate this point, consider the dependence of the index of refraction of the extraordinary wave in a uniaxial crystal on the angle θ between the propagation direction and the crystal optic (z) axis. In terms of normal surfaces for ordinary and extraordinary rays, as shown in Fig. (3.5–1) for a negative uniaxial crystal ($n_e < n_0$).

It can be shown that the index of refraction for an extraordinary wave is given by[Ya75]

$$\frac{1}{n_e^2(\theta)} = \frac{\sin^2\theta}{n_e^2} + \frac{\cos^2\theta}{n_o^2} \qquad (3.5-6)$$

If $n_{2\omega}^e < n_\omega^o$, there exists an angle θ at which $n_{2\omega}^e(\theta) = n_\omega^o$; so if the fundamental beam (at ω) is launched along θ_m as an ordinary ray, the second-harmonic beam will be generated along the same direction as an extraordinary ray. The angle θ is determined by the intersection between the sphere (shown as a circle in the figure) corresponding to the index surface of the ordinary beam at ω with the index ellipsoid (3.5-6) of the extraordinary ray that gives $n_{2\omega}^e(\theta)$. The angle θ_m for negative uniaxial crystals is, satisfying $n_{2\omega}^e(\theta_m) = n_\omega^o$,

$$\frac{\cos^2\theta_m}{(n_{2\omega}^o)^2} + \frac{\sin^2\theta_m}{(n_{2\omega}^e)^2} = \frac{1}{(n_\omega^o)^2} \qquad (3.5-6)$$

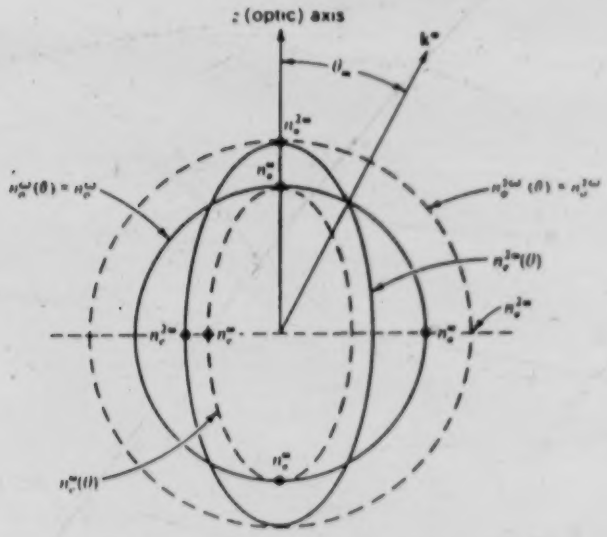

Fig. 3.5–1 Normal (index) surfaces for the ordinary and extraordinary rays in a negative ($n_e < n_0$) uniaxial crystal. If $n_e^{2\omega} < n_0^{\omega}$, the condition $n_e^{2\omega}(\theta) = n_0^{\omega}$ is satisfied at $\theta = \theta_m$.

and, solving for θ_m,

$$\sin^2\theta_m = \frac{(n_\omega^o)^{-2} - (n_{2\omega}^o)^{-2}}{(n_{2\omega}^e)^{-2} - (n_{2\omega}^o)^{-2}} \qquad (3.5-8)$$

This is refered to as the Type I phase matching. The $KDP(KH_2PO_4)$ used in the present experiment falls into this category.

Another point worth describing is the effective nonlinear coefficient d_{eff}. It is necessary to select appropriately the orientation of polarization of the fundamental waves relative to the crystal axes to obtain the maximum conversion efficiency for the generated second harmonic. For simplicity of discussion we take the case of KDP. KDP belongs to the point group $\bar{4}2m$ and is a negative birefringent

crystal. For type I phase matching in KDP ($n_0 > n_e$), two waves are polarized ordinary and the generated polarization is extraordinary. Thus the effective nonlinear coefficient is

$$d_{eff} = -d_{14} \sin\theta \sin 2\varphi \qquad (3.5-9)$$

where we assume a wave propagating at an angle θ to the optic axis and φ to the crystal x axis in a crystal with small birefringence. Obviously to maximize $deff$, φ should be 45° to the x or y axes. Since θ is restricted by the phase matching condition it cannot be maximized. It gives a guide to the way the crystal should be cut.

Two further aspects of phase matching should be considered. They are double refraction and the acceptance angle in the nonlinear interaction.

In an anisotropic crystal the polarization induced by an electric field and the field itself are not necessarily parallel. Thus, as the ordinary wave propagates in a crystal its power flow direction differs by the double refraction angle ρ from its phase velocity direction, as shown in Fig. (3.5-2).

The effect is referred to as Poynting vector walk-off as it leads to a walk-off of the beam energy at an angle ρ. The doubling refraction angle is given by

$$\rho \approx \tan\rho = \frac{n_\omega^o}{2}\{\frac{1}{(n_{2\omega}^e)^2} - \frac{1}{(n_{2\omega}^o)^2}\}\sin 2\theta \qquad (3.5-10)$$

For typical birefringent crystals in the power flow leads to a separation of the extraordinary waves after a distance

$$l_a = \frac{\sqrt{\pi}\omega}{\rho} \qquad (3.5-11)$$

called the aperture length. Here ω is the focussed laser beam electric field radius. For example, for KDP $\rho \sim 1°$ and at $\omega = 0.3mm$ we find $l_a = 6cm$. This is comparable

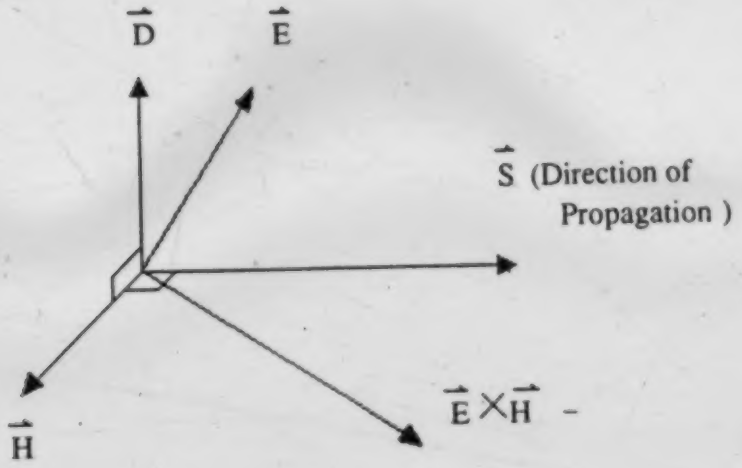

Fig. 3.5–2 The relative orientation of $\vec{E}, \vec{D}, \vec{H}, \vec{s}$ and the Poynting vector, $\vec{E} \times \vec{H}$, in an anisotropic crystal. The vectors $\vec{D}, \vec{E}, \vec{s}$, and $\vec{E} \times \vec{H}$ lie in one plane.

with the $5cm$ of half crystal length in the present experiment . Thus, the generated wave walk-offs appreciably half way through the crystal. This leads to a substantial reduction in SHG efficiency.

The acceptance angle of the nonlinear crystal can be calculated by expanding the argument of the phase synchronism factor $\sin^2(\frac{\Delta kl}{2})/(\frac{\Delta kl}{2})$ in a Taylor series. For SHG

$$\Delta k = \Delta k(\theta = \theta_{match}) + \frac{\partial \Delta k}{\partial \theta}|_{\theta_m} \delta\theta$$

where

$$\Delta k = k_{2\omega} - 2k_{\omega} = \frac{4\pi}{\lambda_{\omega}}[n^{e}_{2\omega}(\theta) - n^{o}_{\omega}]$$

for negative birefringent Type I phase matching. Since at $\theta = \theta_m$, $\Delta k = 0$ we find

$$\Delta k = \frac{4\pi}{\lambda_{\omega}} \frac{\partial n^{e}_{2\omega}}{\partial(\theta)}|_{\theta_m} \delta\theta \qquad (3.5-12)$$

where $n^e_{2\omega}(\theta)$ is given by Eqn.(3.5-6). Carrying out the above differentiation we find

$$\Delta k = \frac{2\pi}{\lambda_\omega}[n^e_{2\omega}(\theta)]^3 \frac{(n^e_{2\omega})^2 - (n^o_{2\omega})^2}{(n^e_{2\omega})^2(n^o_{2\omega})^2} \sin 2\theta \, d\theta \qquad (3.5-13)$$

Evaluating at $\theta = \theta_m$ we have $n^e_{2\omega}(\theta) = n^o_\omega$ so that

$$\Delta k = \frac{2\pi}{\lambda_\omega}[n^e_{2\omega}(\theta)]^3 [\frac{1}{(n^e_{2\omega})^2} - \frac{1}{(n^o_{2\omega})^2}] \sin 2\theta_m \, \delta\theta \qquad (3.5-14)$$

For a crystal with small birefringence this expression simplifies to

$$\Delta k = \frac{2\pi}{\lambda_\omega}(n^o_{2\omega} - n^e_{2\omega}) \sin 2\theta_m \, \delta\theta \qquad (3.5-15)$$

Finally, to find the acceptance angle we note that the $\sin^2(\frac{\Delta kl}{2})/(\frac{\Delta kl}{2})$ function reaches its first zero for $\frac{\Delta kl}{2} = \pi$, being approximately the half width. Using this criterion, half the angular acceptance inside the nonlinear crystal is

$$\delta\theta = \frac{\lambda_\omega}{l(n^o_{2\omega} - n^e_{2\omega}) \sin 2\theta_m}$$

For a 5 cm crystal of KDP at $\lambda_\omega = 600nm$, $\Delta n = 0.05$, $\sin 2\theta_m \approx 1$ we find $\delta\theta = 0.24m\,rad.$. The external acceptance angle is $\delta\theta_{ext} = n\delta\theta = 0.36m\,rad.$. This demonstrates that the angle is rather critical when adjusting the optics. It is therefore necessary to isolate the crystal mount from vibration.

3.6 Focussing

So far, we have assumed that the interacting waves are plane waves. In reality, the laser beam comes out of a cavity which determines the profile of the wave front of the laser beam, usually a Gaussian beam. As seen before, the SHG generation is proportional to the output power of the fundamental wave. Therefore, it is necessary to focus the laser beam onto the crystal to get high conversion efficiency.

The action of focussing causes, in turn, the divergence of the beam after going away from the waist where the wavefront can be taken as plane wave to a first order approximation. Moreover, the double refraction of the uniaxial crystal causes the Poynting vector describing the energy flow (or the ray) to walk off the direction of propagation (given by the wave normal having the same phase velocity), thus reducing the second harmonic efficiency. In the following, we treat focussing for the case of SHG with a Gaussian beam interaction in the near field both with and without double refraction, since the near field approximation applies to most experimental situations.

The fundamental mode or Gaussian mode electric field is described by

$$E(x,y,z) = E_0 \frac{\omega_(0)}{\omega(z)} exp[-i(kz - \varphi)] exp\{-r^2[\frac{1}{\omega^2(z)} + \frac{ik}{2R}]\} \qquad (3.6-1)$$

where

$$\varphi = \tan^{-1}(\frac{z}{z_R}) \qquad (3.6-2)$$

is the phase factor for a TEM_{00} Mode and

$$2z_R = b = \omega_0^2 k \qquad (3.6-3)$$

describes the confocal parameter b as twice the Rayleigh range, z_R. Here R is the beam radius of curvature and $k = 2\pi/\lambda$ is the propagation factor in the medium.

In general the beam radius and wave front curvature as a function of the distance z along the beam propagation are given by

$$\omega^2(z) = \omega_0^2[1 + (\frac{z}{z_R})^2] \qquad (3.6-4)$$

and

$$R(z) = z[1 + (\frac{z_R}{z})^2] \qquad (3.6-5)$$

where ω is the electric field radius at the beam waist at $z = 0$. The far-field ($z \gg z_R$) beam diffraction angle for the fundamental mode is

$$\theta = \frac{\lambda}{\pi\omega_0} \qquad (3.6-6)$$

In the near-field limit $z \ll z_R$ the expression for the TEM_{00} Gaussian beam reduces to

$$E(x,y) = E_0 exp(-\frac{r^2}{\omega_0^2}) \qquad (3.6-7)$$

where $r^2 = x^2 + y^2$. In the limit $\omega(z) \to \omega_0$, $\varphi \to 0$, and $R(z) \to \infty$ so that the fundamental mode is a plane wave with a Gaussian amplitude profile.

The power in the beam is

$$\begin{aligned} P &= \frac{nc\epsilon_0}{2}\int |E(x,y)|^2\, dxdy \\ &= \frac{nc\epsilon_0}{2}\int_0^{2\pi}\int_0^{\infty} |E(r)|^2\, rdrd\varphi \\ &= \frac{nc\epsilon_0}{2}|E_0|^2(\frac{\pi\omega_0^2}{2}) \\ &= I_0(\frac{\pi\omega_0^2}{2}) \end{aligned} \qquad (3.6-8)$$

where I_0 is the peak intensity and $\pi\omega_0^2/2$ is the effective area of the Gaussian beam.

To find the power generated by SGH in the near-field limit we consider the low conversion-efficiency limit. Integrating Eqn.(3.4-13) as before and simplifying the notation

$$E(r) = \kappa E_1^2(r) L \frac{\sin(\frac{\Delta kl}{2})}{(\frac{\Delta kl}{2})} \qquad (3.6-9)$$

We now introduce the radial field variation by letting $E_1(r) = E_1 exp(-r^2/\omega_1^2)$, where ω_1 is the electric field radius of the fundamental field. Thus

$$E_2(r) = \kappa E_1^2 l\, (-\frac{2r^2}{\omega_1^2}) \qquad (3.6-10)$$

where we have assumed $\Delta kl/2 = 0$ and set $\sin(\Delta kl/2)/\Delta kl/2 = 1$. Note that the electric field radius of the generated SHG field is $\omega_1/\sqrt{2}$. Thus the fundamental and SHG fields have equal confocal parameters.

The power generated at the SHG is

$$P_2 = \frac{nc\epsilon_0}{2}\int_0^{2\pi}\int_0^{\infty}|E_2(r)|^2\, r dr d\varphi \qquad (3.6-16)$$

Substituting from Eqn.(3.6-10) and carrying out the integration we find

$$P_2 = \frac{nc\epsilon_0}{2}E_1{}^4\kappa^2 l^2(\frac{\pi\omega_1^2}{4}) \qquad (3.6-12)$$

For a Gaussian mode the power is given by Eqn.(3.6-8) so that

$$P_2 = P_1|E_1|^2\kappa^2 l^2/2 \qquad (3.6-13)$$

or

$$\frac{P_2}{P_1} = P_1\frac{2\kappa^2 l^2}{nc\epsilon}\frac{1}{\pi\omega_1^2} \qquad (3,6-14)$$

In terms of intensity with $I_1 = P_1/(\pi\omega_1^2/2)$ and $I_2 = P_2/(\pi\omega_2^2/2)$ with $\omega_2 = (1/\sqrt{2})\omega_1$, we find

$$\frac{I_2}{I_1} = I_1\frac{2k\kappa^2 l^2}{nc\epsilon_o} = \Gamma^2 l^2 \qquad (3.6-15)$$

which agrees with the previous conversion efficiency derived for the plane wave case given by Eqn.(3.4-17).

We now consider focussing in the near-field but in the presence of double refraction. We again assume perfect phase matching in the low conversion limit and write

$$E_2(x,y,z) = i\kappa\int_0^l E_1^2(x,y)\, dz \qquad (3.6-16)$$

To account for Poynting vector walk-off at an angle ρ we let the walk-off occur in the $x-z$ plane, as shown in Fig.3.6–1 [Bo68], so that observed field coordinates must be related to the generating field by

$$\begin{aligned} y &= y' \\ x &= x' + \rho(l - z') \end{aligned} \qquad (3.6-17)$$

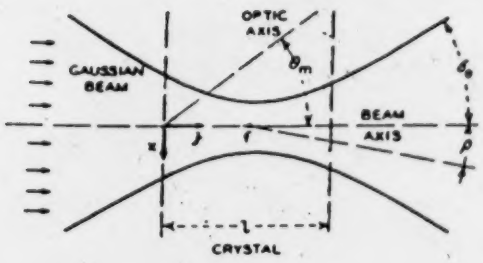

Fig. 3.6–1 Diagram of the Gaussian beam being focussed in a crystal.

Thus Eqn.(3.6-16) becomes

$$E_2(x,y,z) = i\kappa \int_0^l E_1^2[(x - \rho(l-z')), y]\, dz' \qquad (3.6-18)$$

The fundamental driving field has the form

$$E_1(x',y')E_1 exp(-\frac{y'^2}{\omega_1^2}) exp(-\frac{x'^2}{\omega_1^2}) \qquad (3.6-19)$$

Substituting we have

$$E_2(x,y,l) = i\kappa E_1^2 exp(-\frac{2y}{\omega_1^2}) \int_0^l exp[-\frac{2}{\omega_1^2}(x - \rho(l-z'))]^2\, dz \qquad (3,6-20)$$

Introducing a set of normalized coordinates

$$u = \sqrt{2}\frac{x - \rho l}{\omega_1}$$
$$\tau = \sqrt{2}\frac{\rho z'}{\omega_1} \qquad (3.6-21)$$
$$t = \sqrt{2}\frac{\rho l}{\omega_1}$$

and define the integral

$$F(u,t) = \frac{1}{\tau}\int_0^t exp(-(u+t)^2)\, d\tau \qquad (3.6-22)$$

In terms of these parameters Eqn.(3.6-20) becomes

$$E_2(x,y,l) = i\kappa E_1^2 exp(-\frac{2y^2}{\omega_1^2})lF(u,t) \qquad (3.6-23)$$

The integral $F(u,t)$ describes the skewed second harmonic field resulting from double refraction. In the absence of double refraction $\rho = 0$, $F(u,t) = exp(-\frac{2x^2}{\omega_1^2})$ and the generated field reduces to the previous case. For non-zero ρ, $F(u,t)$ leads to generated SH power skewed in the direction of ρ. Fig.(3.6–2) illustrates the generated SHG power as a function of u with t as a parameter [HW77].

A useful parameter for describing the effects of double refraction is the aperture length of Eqn(3.5-11),

$$l_a = \frac{\sqrt{\pi}\omega_1}{\rho} \qquad (3.6-24)$$

The parameter t can be normalized to l_a by

$$t = \sqrt{2\pi}\frac{l}{l_a} \qquad (3.6-25)$$

and thus is a measure of the effects of beam walk-off.

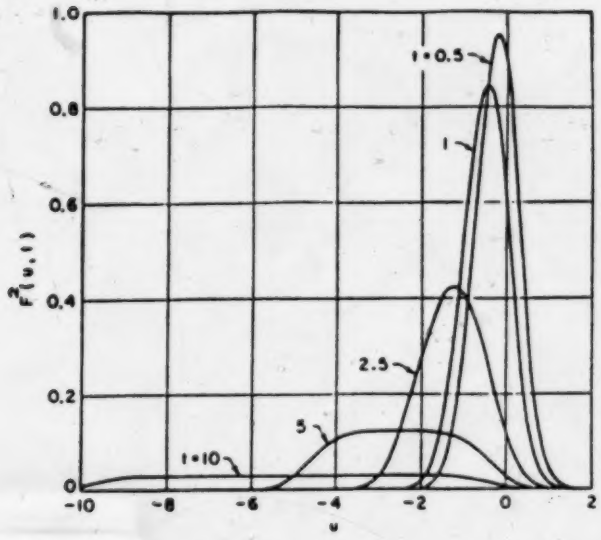

Fig. 3.6–2 The function of $F^2(u,t,q)$ as a function of u for $q = 0$ and several values of t.

To calculate the total SHG power we substitute Eqn.(3.6-23) into the expression for power

$$P_2 = \frac{nc\epsilon_0}{2}\int_{-\infty}^{\infty}\int_{-\infty}^{\infty}|E_2(x,y,l)|^2\,dxdy \qquad (3.6-26)$$

Carrying out the y integral using $\int_0^\infty e^{-a^2x^2}\,dx = \sqrt{\pi}/2a$ we find

$$P_2 = \kappa^2\frac{nc\epsilon_0}{2}E_1^4\frac{\sqrt{\pi}\omega_1}{2}l^2\int_{-\infty}^{\infty}F^2(u,t)\,du \qquad (3.6-27)$$

$$\frac{P_2}{P_1} = \frac{\Gamma^2 l^2}{2}\sqrt{\frac{2}{\pi}}\int_{-\infty}^{\infty}F^2(u,t)\,du$$
$$= \frac{\Gamma^2 l^2}{2}G(t) \qquad (3.6-28)$$

where

$$G(t) = \sqrt{\frac{2}{\pi}}\int_{-\infty}^{\infty}F^2(u,t)\,du \qquad (3.6-29)$$

Fig.(3.6-2) plots $G(t)$ as a function of t. In the absence of walk-off $F(u,0) = exp(-2x^2/\omega_1^2)exp(-u^2)$ and $G(t) = 1$ so that the conversion efficiency again reduces

to that found for the plane wave case. For $\rho \neq 0$, $G(t)$ leads to a reduction in the second harmonic efficiency. $G(t)$ is approxmiately 0.5 for $t = 4$. Thus in the presence of walk-off the beam should be focussed such that

$$\omega_1 \geq \frac{1}{2\sqrt{2}}\rho l \qquad (3.6-30)$$

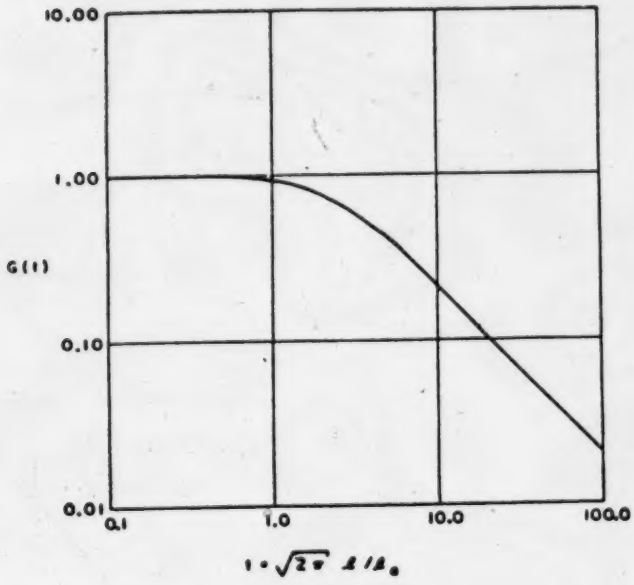

Fig. 3.6-3 The function of $G(t)$ [HW77].

Chapter 4 The Experimental Setup

This chapter outlines the experimental aspects of accelerator-based lifetime measurement with emphasis on the new features of frequency-doubling and charge integration techniques.

4.1 A Brief Outline of the Experimental Setup

The beam-laser technique has evolved from the well-known beam-foil spectroscopy (BFS) technique in which the ion beam from an accelerator bombards a very thin solid foil, usually a carbon foil, in the target chamber and is excited to different stages of ionization. The excited species will decay by fluorescence as the ions move along the beam. The fast moving ion beam not only gives rise to an easy way of detecting the fluorescence in terms of the distance from the excited region, but also to a good time resolution compared to other lifetime measurement techniques.

One problem encountered in BFS is cascading into the level of interest from higher levels, which leads to the detection of several exponential components in the decay curves. This makes it difficult to derive an accurate lifetime from the measured decay curve. In order to overcome this disadvantage, a laser beam may be used to excite the level of interest selectively, thus yielding a single exponential decay curve. A generalized situation is shown in Fig.(4.1–1).

The ion beam velocity, typically about $1mm/ns$, provides the time resolution required to measure lifetimes greater than one or two nanoseconds. The low density of the ion beam and target chamber residual gas avoids the problems of

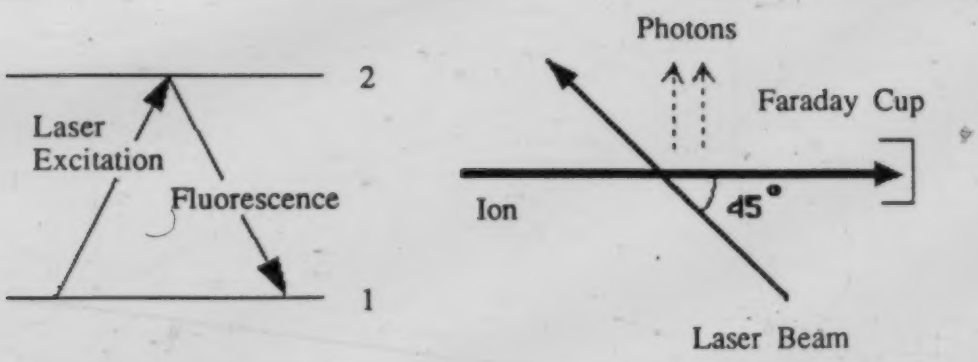

Fig. 4.1-1 Excitation and transition scheme of the laser experiment.

radiation trapping and collisional de-excitation. After leaving the interaction region the number of ions in the excited state (level 2) decays exponentially with time

$$N_2(t) = N_2(0)exp(-t/\tau) \qquad (4.1-1)$$

where $N_2(0)$ is the initial number in the level 2 after excitation. This corresponds to a single exponential decay in the intensity of the monitored transition (2–1) with increasing distance from the interaction region and can then be analyzed by a simple two-parameter least-squares fit to obtain the mean life τ. This apparently ideal experimental situation may be complicated by the presence of a background signal due to collisions of ions in the beam with the residual gas molecules.

To obtain a reasonable signal-to-noise ratio one must have a sufficiently large ion beam current and adequately populate the upper state, as well as minimizing the scattered laser light and ion beam background. The choice of whether to use a continuous wave (CW) or pulsed laser depends on the levels that one wants to study. The high-power pulsed excimer-pumped dye laser used for this research provides the

high power required for the implementation of optical frequency-doubling, which can extend the available wavelengths to the ultraviolet region, while a CW laser is not competent in this respect. Although CW lasers provide a higher signal-to-noise ratio, their application is limited to some neutral species with resonance lines in the visible region.

The intensity decay curves were accumulated by summing several (usually 10–20) successive "sweeps", each sweep being composed of from twenty to thirty datum points corresponding to detection positions separated by 0.5–1.0 mm. This multi-scaling technique reduces the effect of systematic errors (such as a slow drift of laser frequency or power) since each sweep lasts a short time (about 5–10 minutes) compared to the overall collection time for the whole decay curve. Alternate sweeps along the ion beam were made in opposite directions, the sweeps made moving down from the excitation region being summed and analyzed independently of those made moving upstream towards it.

A schematic illustration of the experimental setup is shown in Fig.(4.1–2). It is composed of three main parts: the accelerator system, the laser frequency-doubling system, and the detection system. In the following sections, we will examine each subsystem individually.

The present experiment made use of the $350keV$ linear accelerator equipped with a Danfysik 911A hollow cathode ion source. It is important to maintain the oven of this ion source at a constant temperature to obtain an adequate and stable ion beam. The temperature is controlled by the proximity of the oven to the

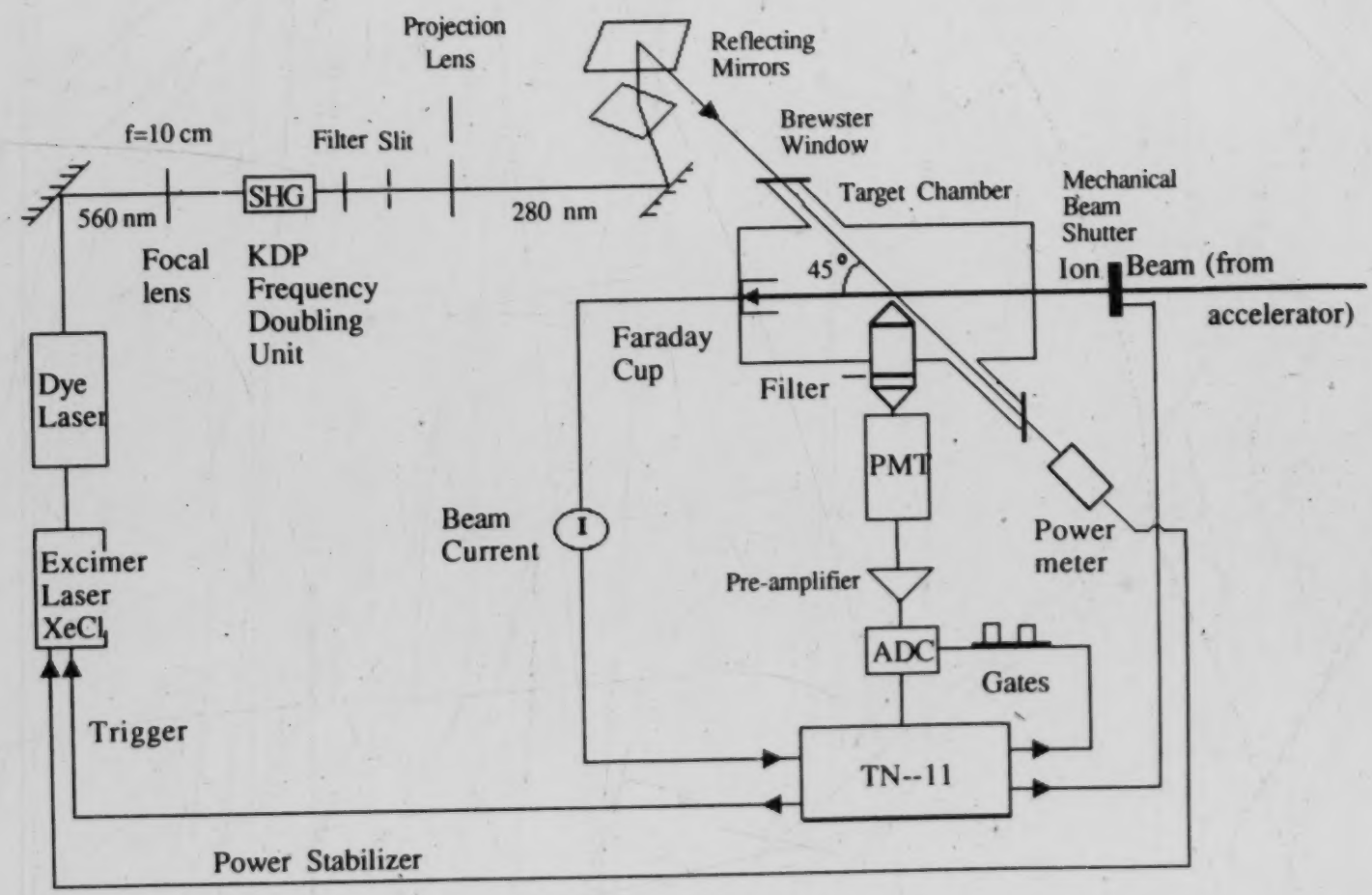

Fig. 4.1-2 Schematic diagram of the experiment setup.

filament. It was necessary to push the oven in very slowly until the desired beam current was reached. Krypton was used as carrier gas.

Good alignment of the ion source with the extraction electrode of the accelerator column was required to obtain an adequate beam current. This was not easy as the alignment was sensitive to how the ion source was reassembled after replacement of the filament and cleaning of the components. Although this alignment could be visually checked without running an ion beam by using a telescope focussed on the source aperture, this could only be done once the filament was hot.

The target chamber is the center of the experiment. Firstly, it facilitates the interaction of the two beams taking place properly. Secondly, it allows an observer to detect easily the information about the interaction. The main features are shown in Fig.(4.1-3).

The beam line within the target chamber was defined by the $8mm$ diameter aperture of the Faraday cup and $5mm$ diameter aperture at the entrance to the chamber. The inside wall of the chamber was painted black. With the entrance and exit windows mounted on a long baffled, blackened tube, it is possible to isolate the sources of scattered light from the detection system.

Scattered light produces one of the direct sources of error of the experiment. Here this scattered light originates from two major sources. One is the scattered light produced by the laser beam when it impinges on the window and other surfaces inside the chamber, as well as on the residual gas molecules. The other is the ion beam excitation due to background gas, which results in a relatively wide

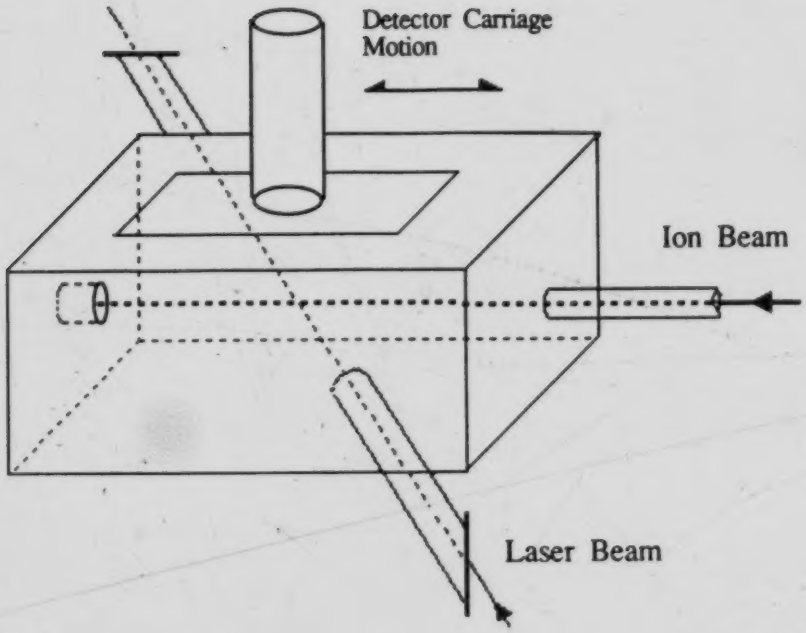

Fig. 4.1-3 Target chamber and detector.

range of wavelengths. Three reflecting mirrors were used to maintain the appropriate polarization of the laser beam relative to the Brewster windows, since the frequency-doubling laser beam is horizontally polarized after the crystal, as described in the previous chapter.

The ion beam background is caused by excitation of all levels of the ions by molecules of the residual gas in the target chamber and vice versa. A low

pressure in the target chamber is vital to minimize the background scattered light as well as the residual excitation of the ion beam. The pressure of the target chamber was usually pumped down to $\sim 1 \times 10^{-6} Torr$.

It is worth considering the way in which the laser beam crossed the ion beam, since it allows one to achieve Doppler tuning. The two beams crossed at 45° which is an adequate compromise between the maximum Doppler shift and the well-defined interaction region which is necessary for the starting point of detection to be close to the excitation region. In the present experiment this Doppler tuning allowed a two-step excitation, 3s–3p and 3p–3d, because of their closely coincident wavelengths, as will be discussed in detail in Chapter 6.

4.2 Laser-frequency-doubling Optics

A recent addition to the excitation source is a KDP crystal, which doubles the input radiation from the Rhodamine 6G dye laser pumped by a Lumonics EPD-330 excimer laser. This permits generation of pulsed tunable radiation around $280nm$ having a typical mean power of $1 - 5$ mW at a repetition rate of 200 Hz, corresponding to a peak intensity at the ion beam of $40 kW/cm^2$. In the present work the incident radiation was focused onto the center of the KDP crystal by using a lens, $L1$, with $10cm$ of focal length. A Corning ($CS7 - 54$,# 9863) glass filter was used to remove the fundamental radiation from the laser beam emerging from the crystal.

It is worth noting that the present phase matching requires that the input radiation is vertically polarized. However, the SHG has horizontal polarization relative to the crystal mount since the SHG is the extraordinary beam. As illustrated

in the last chapter, walk-off of the SHG results in a non-uniform beam spot. In order to achieve a uniform spot at the ion beam, a projection lens plus an aperture were used with the aid of three reflecting mirrors.

The crystal is sealed in an Inrad's Model 562–126 cell, which is purged with nitrogen and hermetically sealed. This cell is seated on a precision gimbal mount specially designed to provide the range of motion and sensitivity required by the Model 562–126. The KDP crystal has a 30 mm interaction length. The aperture, $5.5 \times 12.0mm$, of the cell allows use of the full angular range without vignetting.

Angular tuning of the gimbal in the non-critical direction is accomplished with a thumbscrew-activated tangent arm. The range is $\pm 5°$. Angular tuning in the critical direction is performed by a micrometer-driven tangent arm turntable. The range is $\pm 15°$ with 13 millideg. per micrometer division sensitivity and a 1.3 millideg. vernier. The tuning curve for KDP is shown in Fig.(4.2–1). The most important feature of the present cell is the mechanical stability.

Once having changed the wavelength, it is necessary to adjust the crystal as well as the following optics to maintain a good beam spot at the ion beam. It was found in the present configuration that the crystal must be optimized to have the larger SHG output when scanning the spectra while the beam spot did not move away too much.

4.3 Detection System and Charge Integration

The fluorescence light was collected through the detection optics system moving along the ion beam, firstly away from and then back towards the excitation

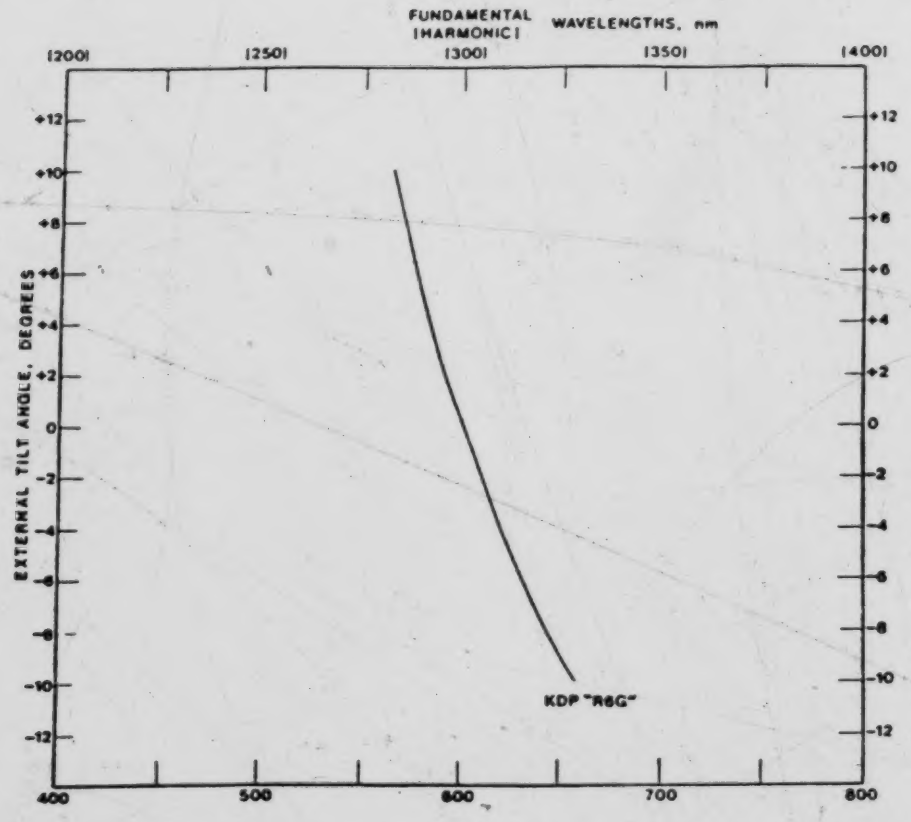

Fig. 4.2-1 Angular tuning curve of KDP with Type I phase matching

region. The schematic diagram is also shown on Fig.(4.1-3), showing the optical axis oriented perpendicular to the plane containing ion and laser beams. Radiation from the ion beam is collimated by a plano-convex lens before leaving the target chamber via a larger rectangular window. It then passes through an interference filter and is focussed by a second lens onto a slit oriented parallel to the laser beam and placed before the photomultiplier tube. The two lenses have equal focal lengths and thus this system defines a $1mm/\cos\varphi$ observation width along the ion beam. The window and the two lenses are of optical quality synthetic fused silica having a useful operation range from about $240nm$ to $2.0\mu m$.

Another problem encountered in moving the detection optics is the alignment of ion beam and the optics. The movement of the detection system to obtain a decay curve does have some drawbacks. The first is the possibility of misalignment between the internal and the external drive screws. That is, although both are driven by the same stepping motor through an appropriate arrangement of gears and thus will travel the same distance, they may not travel in exactly the same direction. Second, even if these two are parallel, they may not be parallel to the direction of the ion beam. Finally, the ion beam diverges slightly, on the order of tenths of a degree, as it travels down the target chamber. All of these imply that the inevitable variation over the observation region will result in some systematic change in measured intensity with changing position along the ion bean, even if the fluorescence intensity is constant.

The alignment procedure and the test of the alignment were discussed in detail in the previous work of this laboratory [Go88]. It shows no systematic variation at about the 0.2% level using residual gas excitation of N_2^+ beam over $70mm$.

The fluorescence photons impinging on the photocathode of the photomultiplier generate photoelectrons, which are amplified through the secondary emission of electrons of the dynodes of the photomultiplier to form a charge pulse at the output. The height of the pulse is proportional to the number of photons incident on the cathode. Usually, the single photon-counting technique is used, which assumes that no more than one photon comes to the photocathode from a single laser pulse, which is very much shorter than the time resolution of the photomultiplier.

Statistically, there exists a probability of collection of more than one photon from a single laser pulse, leading to the so called pile-up: one riding on another

successively. When this is the case, however, the circuit still responds with a single pulse. In order to avoid this pile-up, the gated charge-integration technique was used in the present experiment.

Since the photomultiplier is essentially a charge producing device, the amount of charge produced is proportional to the number of photons incident on the photocathode. A pre-amplifier is a device that integrates all the charge carried by the incoming pulse on a capacitor C_f, whose capacitance is well defined, as shown in Fig.(4.3-1).

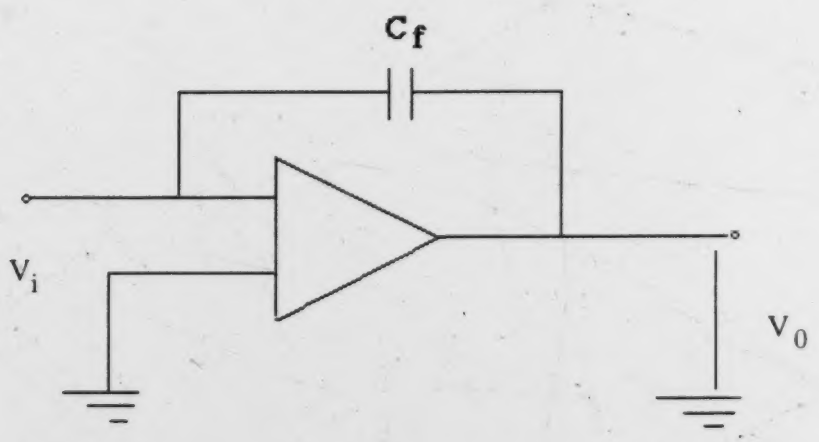

Fig. 4.3-1 Schematic diagram of a charge sensitive amplifier

By working out the voltages from the diagram, it can been seen that the output voltage, V_0, is always proportional to [Le87]

$$V_0 \simeq -\frac{Q}{C_f} \qquad (4.3-1)$$

where Q is the charge on the capacitor C_f. Therefore, several photons can be detected per laser pulse as long as the detector is not saturated. Furthermore, this approach gives a wider dynamic range and permits recording of the fluorescence decay curves over a wider range of intensity than had been possible previously. Thus, in the present experiment, it was possible to record signals over the range from 10 photons per laser pulse down to 0.03 photons/pulse, which was the background level resulting from a combination of residual gas excitation by the $5\mu A$ ion beam and scattered laser light. With single-photon counting, the maximum signal rate that could be used before uncertainty in the pile-up correction made a significant contribution to the overall error estimates, was around 0.3 photons/pulse.

Chapter 5 Data Collection and Analysis

5.1 Data Collection

The signal from the photomultiplier tube was routed to a preamplifier to integrate the total charge, where it was shaped and then sent to a gated analog-to-digital converter (ADC). This digitized each signal as a number , which was summed in our TN-11 data acquisition system. The summation was typically over 2000 laser pulses for each data point in a decay curve. The number of photons corresponding to each digitized charge was determined, either by measuring the signal for single photon events from low intensity thermal light sources or from the single photon height distribution obtained from the ADC.

Each data set was accumulated using the multi-scaling technique in which several successive sweeps were summed. Each decay curve contained a total of 29 data points. The accumulation time for each datum point was 10 seconds, half of which was spent on measuring the background signals with the ion beam turned off. This process made data collection more efficient since, if any problem arose, only one sweep rather than the whole data set was lost. In addition, multi-scaling also reduced the effect of any systematic time variations in the signal. Usually, the decay curves were taken by moving down stream from the interaction region by 0.8 mm steps. Laser power dropping is one of the systematic sources of error. The power dropped dramatically upon refilling the laser. However, it would stabilize after operation for a period of an hour. It was found important to collect the data only after the power had stabilized. The data were also collected when the detector reversed to move toward the interaction region after completing a downstream decay curve. This

double-checked the possible misalignment of the ion beam with the direction of travel of the optical system, as well as the backlash of the driving mechanism of the carriage. Moreover, it also monitored any laser power drop and was an indication of the overall linearity of the detection system according to the symmetry of the two curves.

5.2 Timing sequence

Since the laser operated in a pulse mode, it was possible to use a gating technique to reduce the noise: detector dark counts, ion beam background and scattered laser light. The gating pulse was synchronized with the laser pulse and acted on the ADC. The length of the gating pulse was made large enough to allow for time jitter in the start of the laser pulse ($\pm 10ns$), decay curves extending over at least three lifetimes and the longest rise-time of the electronic components. In all cases the gating pulse was short enough so that the detector dark count rate was negligible.

The gating pulses were used for the different purposes in the designated time sequence, as shown in Fig (5.2-1). The time sequence was generated in the computer. First, when the beam was on (beam shutter is open), a triggering pulse was routed to fire the laser, and a simultaneously generated switch pulse activated the counter (fast scaler) in the computer to make sure that it was ready to read the incoming pulse of the output of ADC and to store the count in an appropriate channel. After $1.2\mu s$, a gating pulse of $1.7\mu s$ width activated the ADC to start processing the total signal A. Since the laser repetition rate used was 200 Hz, the time interval between two adjacent A gates was 5 ms. This interval was used to record the beam background using the B gate, which had the same width as gate A and occurred approximately 1 ms after the immediately previous A gate. Thus, the total signal

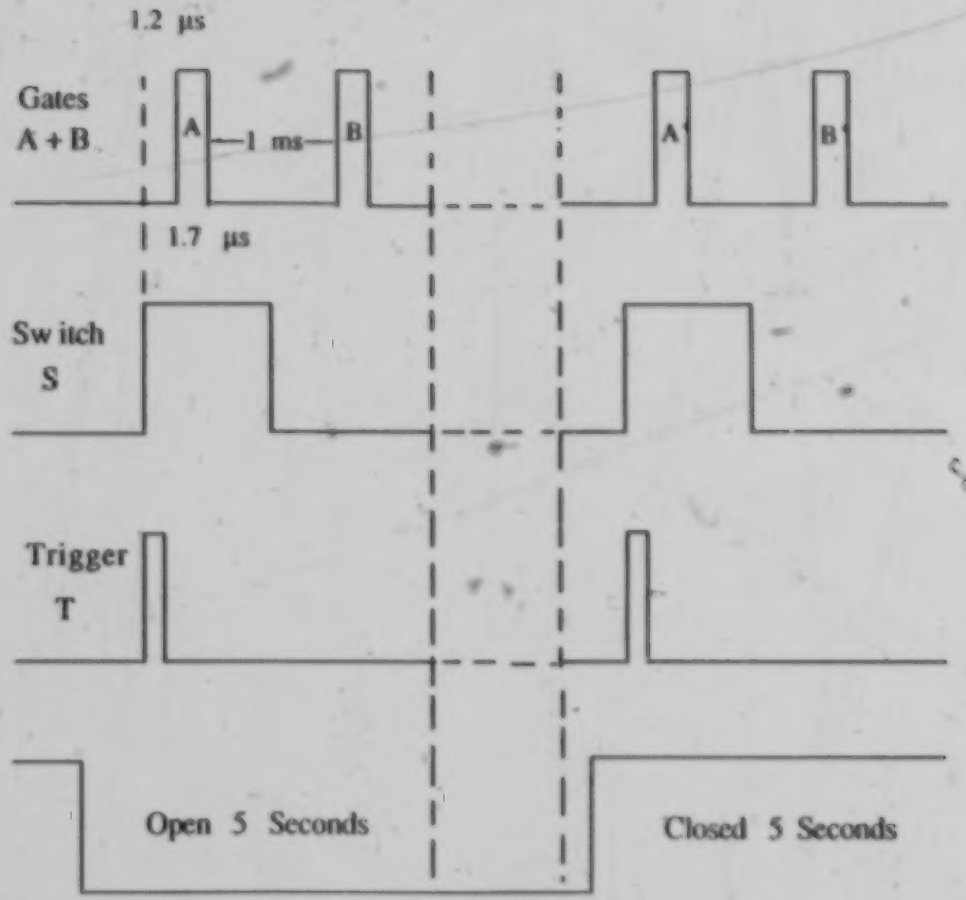

Fig. 5.2-1 Timing sequence.

and beam background were recorded alternately in one half of the time used for a particular datum point. When this half of the time was over, the beam was blocked by using a mechanical shutter. The laser scattered light, A′, and the dark count, B′, arising from residual gas excitation or the noise of the detector and the electronic components, were recorded alternately in the same manner as for the previous two. In summary, at each point of the decay curve the signal was accumulated for a fixed time (*i.e.* a fixed number of laser pulses) for each of the following conditions:

(A) Laser beam on, ion beam on (Total Signal)

(B) Laser beam off, ion beam on (Beam Background)

(A′) Laser beam on, ion beam off (Laser Background),

(B′) Laser beam off, ion beam off (Dark Counts).

3.3 Normalization

The ion beam current was recorded simultaneously during the same fixed time as A and B to account for fluctuations. It was also digitized to be used as a normalization to the final counts. Even so, the maximum permitted magnitude of the fluctuations was chosen to be no more than 5% to avoid extra error. Otherwise, the ion beam was optimized for stability before carrying on to the next sweep.

In addition, the ungated beam background(UBB) was measured when necessary to check residual gas effects and beam background. This also provided an additional benefit for the test of the alignment between the detection system and ion beam.

5.4 Fitting the Single-Exponential Decay Curve

Having obtained the single-exponential decay curve, we need to derive the lifetime accurately from it. Before doing this, it is necessary to substract out the background signal and normalize the result. For the i^{th} data point, we have the decay signal:

$$S_i = [(A - B) - (A' - B')] \times \frac{\bar{N}}{N_i} \qquad (5.4-1)$$

where N_i is the normalization for the i^{th} data point and $\bar{N}$ is the mean value of the normalization signal.

The variance of S is estimated assuming that

1. There is no error in the normalization;
2. A, B, A', and B' follow Poisson statistics and their random variations are not correlated.

Therefore,

$$var(S_i) = (A + B + A' + B') \times (\frac{\bar{N}}{N_i})^2 \qquad (5.4-2)$$

The pure decay signal decays exponentially with increasing distance from the excitation region so that

$$\begin{aligned} S_i &= Ae^{\alpha(x_i - x_1)} \\ \alpha &= \frac{1}{v\tau} = decay\ \ length \\ A &= amplititude\ at\ x_1. \end{aligned} \qquad (5.4-3)$$

The coefficients A and α and associated uncertainties δA and $\delta\alpha$ are determined using a standard least-squares fit [Be69] to the linear equation.

$$Y_i = \ln S_i = (\ln A) - \alpha(x_i - x_1) \qquad (5.4-4)$$

The fit is weighted according to the inverse of the variance of the Y_i:

$$var(Y_i) = var(\ln S_i) = \frac{var(S_i)}{S^2} \qquad (5.4-5)$$

Although the starting point of a decay curve is chosen to begin as close as possible to the interaction region in order to obtain a high count, points from this region are truncated to test for any systematic variation of the lifetimes when fitting the curve. The fitting program also provides the scatter-plots as an indication of any systematic deviation of the fitting function from the actual data. The fit itself gives only the statistical error in the lifetime,

$$\frac{\delta\tau_i}{\tau_i} = \frac{\delta\alpha_i}{\alpha_i} \qquad (5.4-6)$$

which reflects the random sources of error such as the Poisson distribution of the counts as well as the fluctuations in the laser power and ion beam.

For each run, the fitting program produces its best estimate for the lifetime (τ_i) and the error $\delta\tau_i$ associated with it. Ideally, on average, the reduced chi-squared is equal to 1. If it is larger than 1 and the data points distribute randomly on both sides of the fitting curve, then it is most likely that the error for each datum point is underestimated. The relative weighting for each point is right but the absolute weight is wrong. In order to take account of this, the uncertainty in each datum point is multiplied by the square root of the average reduced chi-squared. This has the effect of bringing the reduced chi-squared value down to 1 and also of multiplying the uncertainty in the lifetime by the square root of the original reduced chi-squared.

Weighting each individual measurement of the lifetime in terms of its modified uncertainty, $\delta\tau'$, the mean lifetime ($\bar{\tau}$) is obtained,

$$\bar{\tau} = \frac{\sum \tau_i \omega_i}{\sum \omega_i} \qquad (5.4-7)$$

The standard error of this mean is given by

$$\delta\tau = \left(\frac{1}{\sum(1/\delta\tau_i')^2}\right)^{1/2} \qquad (5.4-8)$$

where $\omega_i = (1/\delta\tau_i')^2$.

The standard deviation of the lifetime can be obtained by

$$\delta\tau_{sd} = \left[\frac{N\sum[\omega_i(\tau_i - \bar{\tau})^2]}{(N-1)\sum\omega_i}\right]^{1/2} \qquad (5.4-9)$$

which is an indication of the width of the distribution of the lifetimes for each individual fit about the mean. It is worth noting that the lifetime estimate allowing for statistical factors only is based on Eqns.(5.4-7) and (5.4-8) instead of (5.4-9).

Examples of results obtained from a single data set are shown in Table. (5.4-1), where the different fitting methods are compared. The last column on this table shows truncations. Fits A and B have the first 29 points truncated so that only the second half (up stream) of the decay curve is analyzed. On the contrary, fits E and F are for the analysis of the first half (down stream). In between are the entire data set fittings with 3 points truncated at each end of the decay curve. Ideally, the decay curve could be well-fitted with a single exponential. This is a two-parameter fit. It is useful to include an additional constant in the fit, as seen in the second last column on the table, as a test of possible systematic effects on the decay curve. For the present case, all the results overlap within their deviations (multiplied by the square root of their reduced chi-squared as discussed above). In this data set, the constant is positive. Other data sets give negative constants. There is no evidence of systematic error here. Therefore, the consistency of the signs of the constant for

Table. 5.4-1 Comparision of different fitting methods

λ	Energy	Run #	Lifetime	Standard	Reduced	Added	Truncated
280.3 nm	keV	# Fit	τ (ns)	Deviation	$-\chi^2$	const.	Front; Rear
	330	3 A	3.8191	0.0271	3.429	none	29; 3
	330	3 B	3.7944	0.0608	3.570	+ve	29; 3
	330	3 C	3.7503	0.0424	2.888	+ve	3; 3
	330	3 D	3.8142	0.0193	2.885	none	3; 3
	330	3 E	3.8092	0.0276	2.070	none	3; 29
	330	3 F	3.7077	0.0591	2.008	+ve	3; 29

the same data set demonstrates also that the fitting methods give consistent results in terms of the statistical uncertainties.

5.5 Systematic Sources of Error

Each experimental environment is also subject to systematic error. Perhaps it is one of the most difficult things for the experimentalist to determine. For the beam-laser experiment, several sources of systematic error from different sections of the system will be examined according to their significance with regard to the accurate determination of the final lifetime.

As mentioned earlier, good time resolution of the beam-laser technique is attributed to the fast moving ion beam. Therefore, the well-defined ion velocity is crucial to the accurate determination of lifetime. This is obvious from

$$\alpha = \frac{1}{v\tau} \qquad (5.5-1)$$

$$\frac{\Delta\alpha}{\alpha} = \frac{\Delta v}{v} + \frac{\Delta\tau}{\tau} \qquad (5.5-2)$$

It is seen that the uncertainty of velocity, $\Delta v/v$, can render a large error to the lifetime even if a good fit ($\Delta\alpha/\alpha$) is obtained.

The velocity is calibrated to $\pm 0.5\%$ using the Doppler effect as well as the two-step excitation which will be discussed in Chapter 6. It turns out that the uncertainty in the velocity is one of the most significant sources of systematic error.

The second error concerns the laser power drop. It tends to shorten the lifetime for decays measured moving away from the excitation region. This effect can be treated as follows. Suppose that the true lifetime is τ_0 and hence the ideal decay curve (Curve I) should be

$$I_1 = Ae^{\frac{-t}{\tau_0}} \qquad (5.5-3)$$

being ploted as curve I in Fig.(5.5–1). Since the power drop is small and we assume that it decreases slowly with time, the resultant (or measured) decay signal may then be expected to be as

$$I_2 = A(1-\beta t)e^{\frac{-t}{\tau_0}} \qquad (5.5-4)$$

as shown being Curve II in Fig.(5.5–1), where β is a small quantity.

In order to estimate the maximum deviation of lifetime obtained by fitting into (5.5–1)(Curve II) from the true value τ_0 (Curve I), another decay curve (Curve III) is chosen in such a way that it has same value at the starting point ($t = t_i$, point B) as the other two but a shorter lifetime τ_0' which cause it to intersect with curve II at the end of the curve ($t = t_f$),

$$I_3 = Ae^{\frac{-t}{\tau_0'}} \qquad (5.5-5)$$

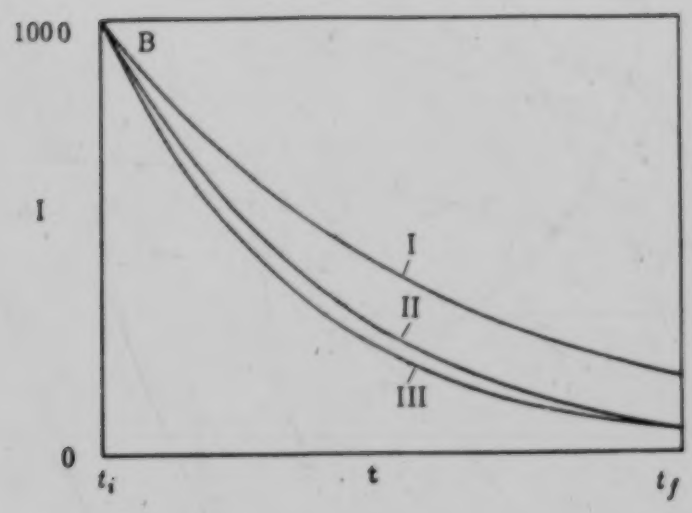

Fig 5.5–1 Effect of the laser power drop on the decay curve

and

$$I_2(t = t_f) = I_3(t = t_f) \qquad (5.5-6)$$

In fact, this is the closest fit to the measured decay (Curve II). (The difference between Curves II and III is exaggerated in Fig.(5.5-1) for clarity.)

Substituting Eqns.(5.5–4) and (5.5–5) into (5.5–6), we have

$$(1-\beta t)e^{\frac{-t}{\tau_0}} = e^{\frac{-t}{\tau_0'}} \qquad (5.5-7)$$

Since β is a small quantity, we then have

$$\frac{1}{\tau_0'} = \beta + \frac{1}{\tau_0} \qquad (5.5-8)$$

or,

$$\frac{\tau_0' - \tau_0}{\tau_0} = -\tau_0'\beta \qquad (5.5-9)$$

In the experiment, the power decreased by 1% for a curve; therefore,

$$\beta t_f = 1\% \qquad t_f = 14ns \tag{5.5-10}$$

or,

$$\beta = 0.07\% \tag{5.5-11}$$

Putting this back into Eqn.(5.5-9) and taking $\tau_0' \approx \tau_0 = 4ns$ yields

$$\frac{\tau_0' - \tau_0}{\tau_0} = -0.29\% \tag{5.5-12}$$

Therefore, most conservatively, the maximum uncertainty of the life-time due to a 1% power drop is -0.29% for sweeps recorded moving away from the excitation region. Similarly, the maximum uncertainty for sweeps recorded moving towards the excitation region due to a 1% power drop is $+0.29\%$.

Another source of error comes from the system dead time, i.e. the finite time required by the system to process one event. Usually, it depends on the duration of the pulse as well as each element in the system. For the sake of simplicity, suppose that the system has a dead time ΔT for all events and is insensitive during this period. The system registers k counts in a time T for the true count rate m. Therefore, the total dead time is $k\Delta T$ during this period, and a total of $mk\Delta T$ counts could be lost. The true number of counts is

$$mT = k + mk\Delta T \tag{5.5-15}$$

Solving for m in terms of k, we have

$$m = \frac{k/T}{1 - (k/T)\Delta T} \tag{5.5-16}$$

or, the observed count rate $n = k/T$,

$$n = k/T = \frac{m}{1 + m\Delta T} \qquad (5.5-17)$$

Eqns.(5.5–16) or (5.5–17) relates the true count rate m to the observed rate $n = k/T$.

Usually, $m\Delta T$ is a small quantity and hence Eqn.(5.5–7) can be expressed as

$$n \simeq m(1 - m\Delta T) \qquad (5.5-19)$$

It is seen from here that the fraction of count lost is proportional to the count rate itself to a first order approximation. Therefore, it is negligible when the count rate is small. This is important for the correction of the decay curve.

In the following, the above discussion will apply to the discussion of a decay curve to obtain the maximum uncertainty of lifetime due to the dead time.

Suppose that an ideal decay curve (no dead time) can be expressed as

$$I_4 = Ae^{\frac{-t}{\tau_0}} \qquad (5.5-20)$$

as shown in Fig.(5.5–2) as Curve I_4.

Because of the dead time, the decay curve (measured) will be

$$I_5 = Ae^{\frac{-t}{\tau_0}}(1 - Ae^{\frac{-t}{\tau_0}}\Delta T) \qquad (5.5-21)$$

being Curve 5 in Fig. (5.5–2). Since the dead time correction is non-linear, the curve has a larger correction in the beginning than at the end. We could have a good fit to I_5 such that

$$I_6 = Ae^{\frac{-t}{\tau_6}}(1 - A\Delta T) \qquad (5.5-22)$$

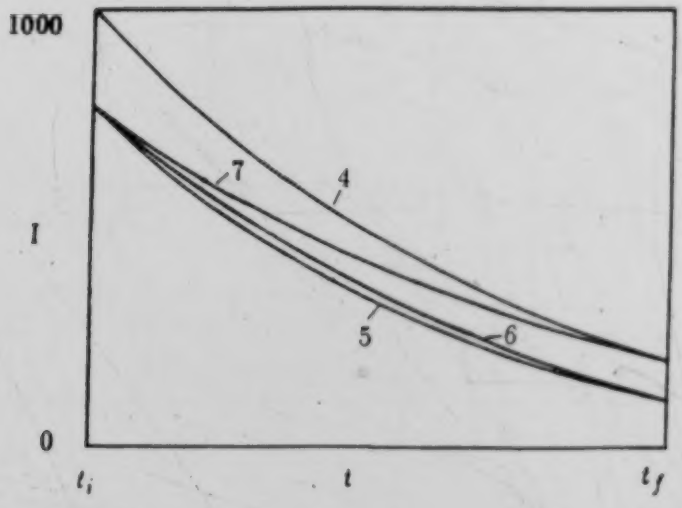

Fig.5.5-2 Effect of the dead time on the decay curve

with

$$I_6(t = t_f) = I_5(t = t_f) \qquad (5.5-23)$$

However, if we constructed a curve in such a way that

$$I_7 = A(1 - A\Delta T)e^{\frac{-t}{\tau_0}} \qquad (5.5-24)$$

with

$$I_7(t = 0) = I_5(t = 0) \qquad (5.5-25)$$

$$I_7(t = t_f) = I_4(t = t_f) \qquad (5.5-26)$$

it would give us an easy way to estimate the error analytically. Then, the difference of the lifetimes between I_7 and I_4 is larger than that between I_5 (or I_6) and I_4. Therefore, finding the difference of the lifetimes between I_7 and I_4 will give the maximum possible error when fitting I_5.

Combining Eqn.(5.5-24, 25, 26) with Eqns(6.5-20, 21) yields

$$\frac{\tau_0' - \tau_0}{\tau_0} = \frac{A\Delta T}{t_f}\tau_0' \qquad (5.5-27)$$

Take $\tau_0' \simeq \tau_0 = 4ns$, $t_f = 14ns$, $A\Delta T = 17000 \times 600 = 1\%$ (maximum dead time in the experiment), we have

$$\frac{\tau_0' - \tau_0}{\tau_0} = 0.29\% \qquad (5.5-28)$$

Thus, the maximum increase of the lifetime due to dead time is by 0.29%.

Table. 5.5-1 Systematic sources of error

Velocity	±0.5%
Laser power drop	±0.29%
Dead time	+0.29%
Misalignment	−0.06%
Quantum beat	−0.004%
Residual gas de-excitation	−0.03%
Net increase : +0.196%	
Systematic error (added in quadrature): ±0.65%	

There are other sources of systematic error: such as misalignment, residual gas de-excitation, etc. They have been worked out previously [Go88] and summarized in Table. (5.5-1). The net increase is used to correct the mean lifetime obtained by Eqn.(5.4-7). The overall systematic uncertainty is given by the square

root of the sum of each in quadrature. Finally, combining this result with the statistical uncertainty from Eqn.(5.4-8) produces 0.96% $\simeq$ 1%, as the overall accuracy of the final result.

Chapter 6 Lifetime Measurements for the 3p Levels of Mg II and an Observation of Two-Step Photon Excitation

This chapter discusses the lifetime measurement results for the 3p levels of Mg II. A comparison of the present work with other previously obtained results is made both for theoretical calculations and experimental values. The second part of this chapter presents an observation of the fluorescence following two-step photon excitation using Doppler tuning, as well as of direct two-photon excitation.

6.1 Lifetime of the 3p levels of Mg II

Using the method and techniques detailed in the preceding chapters, decay curves were recorded at a variety of beam currents and two different velocities. For the Mg^+ ion, $5 - 10\mu A$ could be obtained with the accelerator operating at 250 keV - 330 keV. Most of runs were done at about $7\mu A$ ion beam current with an ion energy of 330 keV. A typical decay curve is shown in Fig.(6–1). It demonstrates how pile-up affects the observed signal and is corrected by the charged integration technique. Each data set was composed of the sum of 5 sweeps under the same experimental conditions. This data set was then analyzed to find one value for the lifetime.

The average power of the frequency-doubled radiation produced could be adjusted from 1 to 5 mW, either through changing the focal length of the lens in front of the KDP crystal or by varying the input excimer-dye laser power. In the experiment, 2 mW average power was found sufficient to saturate the $7\mu A$ ion beam. The repetition rate of the laser was 200 Hz. The beam was projected at the target

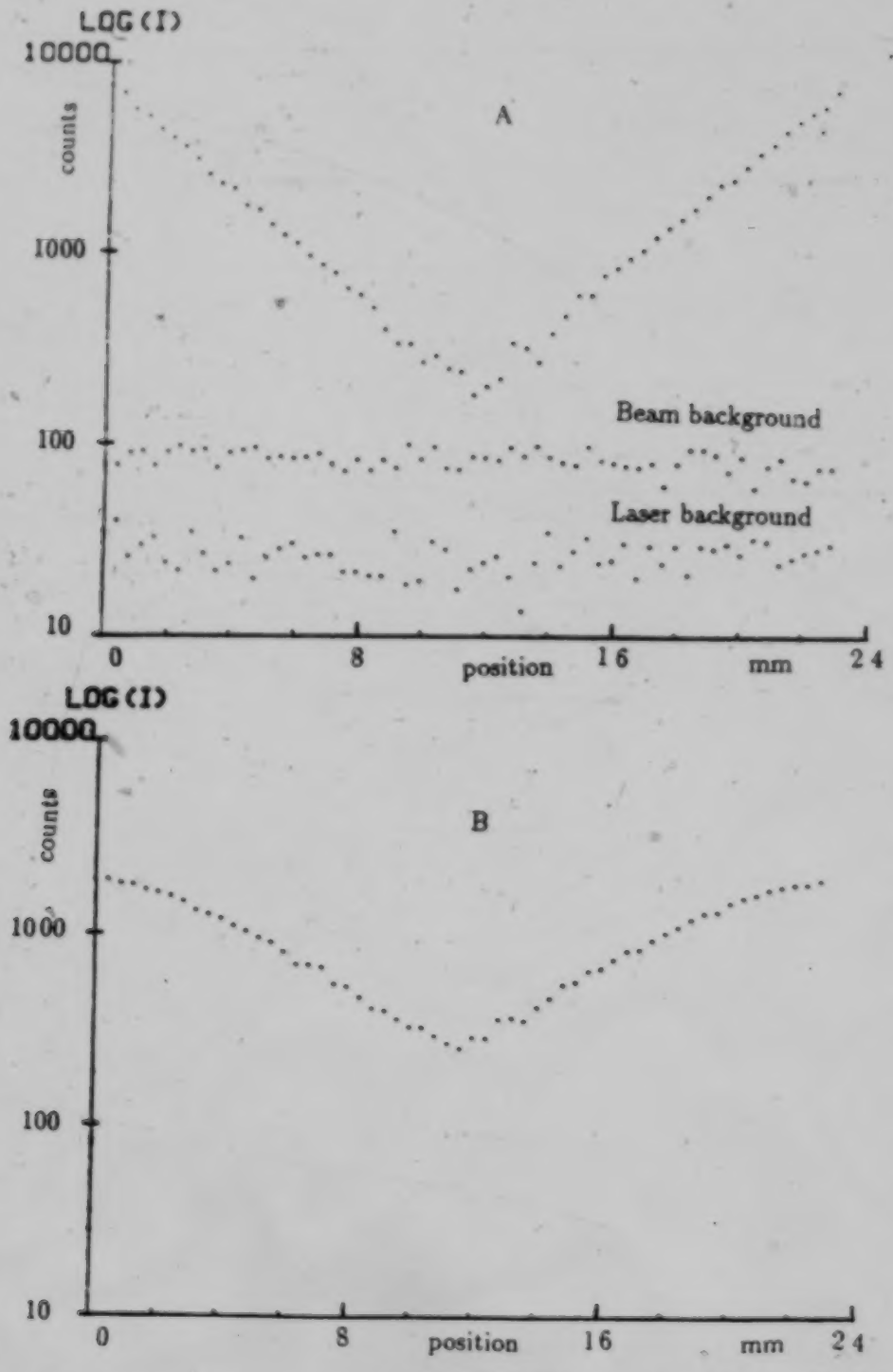

Fig. 6.1-1 A sample decay curve. A) with charge-integration and B) with photon counting.

chamber with an approximately uniform spot size, $5mm \times 2mm$. In terms of the above conditions, the peak pulse intensity at the excitation region was approximately $10 - 40 KW/cm^2$. The laser power was also monitored at the exit window of the target chamber.

The entrance slit of the detection system was 1mm wide. The normalization for a data point in a decay curve was 2000 laser pulses, corresponding to ten seconds. Recording both down and up stream decay curves took approximately 10 minutes for each sweep. For a data set of 5 sweeps, around 50 minutes were needed. The target chamber was pumped down to 1×10^{-6} Torr prior to recording the data and maintained at $1 - 1.5 \times 10^{-6}$ Torr during the course of data collection.

Mg also has two much less abundant isotopes: ^{25}Mg and ^{26}Mg. Optimizing the operation of the ion source, around $0.5 \mu A$ ion beams were obtained for them using 250 keV. The decay curves for them also were recorded and analyzed, which gave the results of 3.75 ± 0.15 and $3.81 \pm 0.10 ns$ for ^{25}Mg and ^{26}Mg, respectively. The larger uncertainty was due to the relatively smaller ion beam and hence a lower signal-to-noise ratio.

The decay curves were analyzed and the uncertainties estimated using the techniques described in the previous chapter. The results from individual runs are shown in Tables. 6.1-1 and 6.1-2 for $^2P_{3/2}$ and $^2P_{1/2}$ respectively, taking account of the reduced chi-squared values (as discussed in Section 5.4) to obtain the mean lifetimes and their uncertainties. The results shown in Table (6.1-3) were obtained by considering the sources of both statistical and systematic errors. In addition, the table contains previous experimental and theoretical values. It can be seen that the present

results agree with previous measurements within their much larger uncertainties. One important thing is that the present work gives a separate value for each level of the doublet, which was not the case for most previous measurements. This reflects the much higher spectroscopic resolution permitted by the use of lasers. One recent calculation done by Theodosiou and Curtis[TC88] shows good agreement with ours. They attributed their results to the careful inclusion of a core polarization potential for which parameters needed to be obtained either from the Hartree-Slater approximation or from an iterative process justified by the experimental binding energy. It seems that their work is better for describing the interaction between the active electron and the core as the number of electrons within the core increased.

Table. 6.1-1 Summary of lifetime measurements for $^2P_{3/2}$

λ	Energy	Run #	Velocity	Lifetime	Standard	Reduced	Truncated
279.6 nm	keV		mm/ns	τ (ns)	Deviation	χ^2-	Front; Rear
	330	7	1.629	3.7759	0.0463	1.208	3; 3
	330	6	1.629	3.7525	0.0306	2.884	3; 3
	250	3	1.418	3.8739	0.0261	3.147	3; 3
	250	2	1.418	3.8693	0.0374	1.931	3; 3

Weighted mean of lifetimes: $\tau = 3.826$ ns

Standard error of this mean: $\delta\tau = \pm 0.025$

Table. 6.1-2 Summary of lifetime measurements for $^2P_{1/2}$

λ,	Energy	Run #	Velocity	Lifetime	Standard	Reduced	Truncated
280.3 nm	keV		mm/ns	τ (ns)	Deviation	χ^2	Front; Rear
	330	4	1.629	3.9946	0.0472	1.188	4; 3
	330	3	1.629	3.7503	0.0424	2.888	3; 3
	330	2	1.629	3.8705	0.0451	2.537	3; 3
	330	1	1.629	3.8338	0.0572	2.467	3; 3
	250	5	1.418	3.9113	0.0271	2.143	4; 4

Weighted mean of lifetimes: $\tau = 3.881$ ns

Standard error of this mean: $\delta\tau = \pm 0.027$

6.2 An Observation of the Fluorescence of Two-Step Excitation

The close coincidence of two wavelengths for the transitions of the 3s–3p and 3p–3d allowed us to make two interesting observations. The first was the two-step excitation, i.e. excitation of the $^2D_{3/2}$ level via the first step excitation of the $^2P_{1/2}$ level. One way to do this using a single laser was to make use of Doppler tuning. With the two beams crossing at 45°, a red shift of a laser line 279.67 nm gave the resonance of $^2P_{1/2}$ level at 280.27 nm; and a blue shift gave the resonance for the $^2D_{3/2}$ at 279.08 nm upon reflecting the beam back by a mirror set up outside the Brewster window. Essentially, this was based on appropriately adjusting the ion velocity. The accelerating voltage was found at 102 keV to give the resonance. One final point is that the path of the reflecting beam needed be deviating slightly from that for the first one, since the ions would travel away as the reflected beam

Table. 6.1-3 Lifetimes of the 3p levels of Mg II

Source	Lifetime (ns)	
	$^2P_{1/2}$	$^2P_{3/2}$
Beam-laser (present work)	3.873 ± 0.037	3.819 ± 0.035
Previous Experiments:		
Hanle Effect [Sim66]		3.67 ± 0.18
Phase Shift [SL71]	3.7 ± 0.5	
Beam Foil [BBB70]	4.5 ± 0.8	
Beam Foil [AP76]	4.2 ± 0.4	
Beam Foil [Lu73]	4.0 ± 0.3	
Beam Foil [Lil80]	4.1 ± 0.4	
Theoretical Estimates		
Dirac Fock [Zi85]	3.75	3.72
Z-Expansion [La75]	3.57	
MCHF [Fi76]	3.86	
Semi-Empirical [Gr78]	3.57	
Semi-Empirical [Gan87]	3.75	
HF + CI [Hi83]	3.78	
HF + CI [Ti88]	3.86	
HS + CP [TC88]	3.872	3.842

was coming back. In order to encounter the excited ions again, it was necessary to direct the reflected beam down stream in such a distance that the round trip time could be compensated. In this experiment, it was around 3 ns. Fig.(6.2-1) shows the fluorescence of 3s-3p transition increasing as the two-step photon excitation was achieved when scanning both the velocity of the ions and the wavelength of the laser.

The increase of the fluorescence was due to the short lifetime of the 3d level so that it would repopulate the level of $^2P_{1/2}$. The decay of this fluorescence for the $^2P_{1/2}$ was also recorded. However, fitting this curve was not as easy as one might expect. This can be understood from the rate equation.

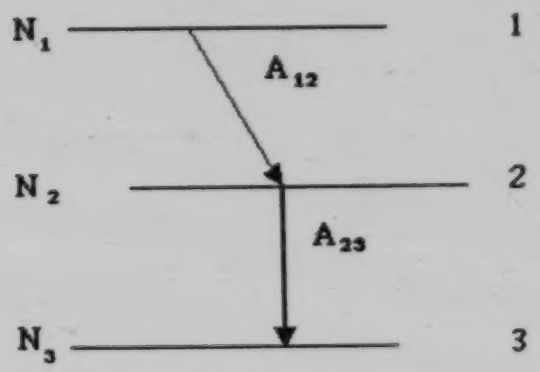

Fig. 6.2-2 Diagram of a three level system.

For the three levels involved,

$$\frac{dN_1}{dt} = -A_{12}N_1$$
$$\frac{dN_2}{dt} = -A_{23}N_2 + A_{12}N_1 \qquad (6.2-1)$$

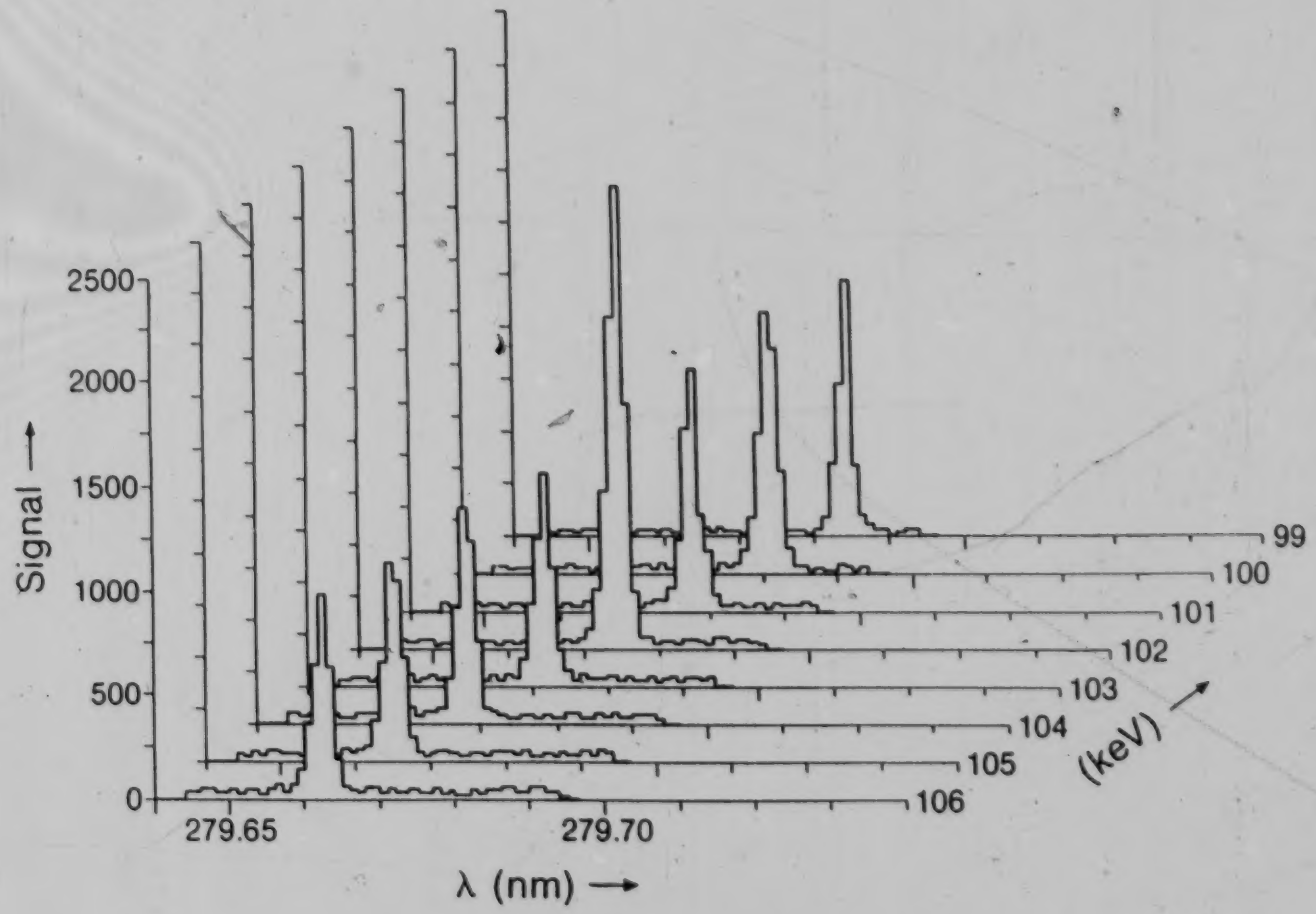

Fig. 6.2–1 An observation of the fluorescence of two-step excitation.

with the initial conditions,

$$N_1 = N_{10} \qquad t = 0$$
$$N_2 = N_{20} \qquad t = 0 \qquad (6.2-2)$$

the general solution for the two levels is

$$N_1 = N_{10}e^{-A_{12}t} \qquad (6.2-3)$$

$$N_2 = (N_{20} + \frac{A_{12}N_{10}}{(A_{12}-A_{23})})e^{-A_{23}t} + \frac{A_{12}N_{10}}{A_{23}-A_{12}}e^{-A_{12}t} \qquad (6.2-4)$$

where $A_{12} = 1/\tau_{(^2D_{3/2})}$ and $A_{23} = 1/\tau_{(^2P_{1/2})}$. It can be seen that the second term in Eqn.(6.2-4) is negative since A_{12} is greater than A_{23}. Because the detector can not distinguish the two coincident wavelengths, the total observed fluorescence signal is

$$\begin{aligned} I &= D(N_1A_{12} + N_2A_{23}) \\ &= DN_{10}\frac{2\frac{A_{23}}{A_{12}}-1}{\frac{A_{23}}{A_{12}^2}-\frac{1}{A_{12}}}e^{-A_{12}t} + A_{21}(N_{20} + \frac{A_{12}N_{10}}{A_{12}-A_{23}})e^{-A_{23}t} \end{aligned} \qquad (6.2-6)$$

where D is an overall response constant of the detection system.

If $\frac{A_{23}}{A_{12}} = 0.5$, the coefficient of the first term in Eqn.(6.2-6) is equal to zero. This means that only the fluorescence from the primary level is observed with an effective population:

$$A_{21}(N_{20} + \frac{A_{12}N_{10}}{A_{12}-A_{23}}) \qquad (6.2-7)$$

Because of the near coincidence of the wavelengths and the high peak laser intensity, the direct two-photon excitation could also be achieved. Using the same beam-crossing geometry as for the two-step excitation (but without reflecting the beam) and taking the Doppler effect into account, a laser wavelength of 279.68 nm was found to pump the $^2D_{5/2}$ level. This wavelength corresponded to the half of the energy between $^2D_{5/2}$ and $^2S_{1/2}$ and gave an intermediate virtual level which was

$16cm^{-1}$ below the level of $^2P_{3/2}$. The detected fluorescence via the $^2P_{3/2}$ level showed that the two-photon excitation had occured. Since the two-photon absorption is a second order effect, the transition probability is much less than that of the first order electric dipole radiation. (It should be mentioned that the present experiment used only one beam, unlike Doppler-free two-photon absorption spectroscopy where every atom absorbs photons of the same energy from two counter-propagating beams.)

Chapter 7 Conclusion

7.1 Conclusion

Using the beam laser technique, the lifetimes of the resonance 3p levels of Mg II have been accurately determined. The overall accuracy from the sources of systematic and statistical error is shown to be better than 1%. This high precision measurement provides a reliable result which can be compared with different theoretical calculations. One point is that the present work has resolved the doublet and given one value for each of the levels, unlike most of the previous experimental and theoretical works, which gave only one lifetime for the unresolved doublet.

The success of the present experiment is attributed to the addition of the frequency-doubling optics, in addition to the high time resolution provided by the beam-laser technique. The pulsed excimer-pumped dye laser has made it possible to use the frequency-doubling technique to extend the wavelength to the U.V. region. The working range could be extended to lower wavelength to study many lines of other elements if a new type of dye and crystal were used.

An order-of-magnitude estimate has been made of the required laser power for saturation to be achieved. The success of this experiment has verified this estimate. Moreover, the observation of the two-step excitation also justifies this point since, otherwise, there would not be enough population in the first excited level to produce the observed large increase of the fluorescence. The accomplishment of the two-photon excitation is also an indication of the laser intensity because the second order effect needs a much stronger field strength.

The spread of beam velocity remains the most significant source of error. In order to obtain a higher accuracy, the accelerator would need to be upgraded. However, even in its present state, there is still room for the study of many other elements at the current level of precision.

As is usually the case in a scientific inverstigation, the experiment has posed new problems in addition to providing some useful results. So far, only the resonance levels of singly ionized ions have been studied using the beam-laser technique since the present hollow cathode type of ion source can only produce such ions. Although two-step photon excitation has been achieved, this does not give a sufficiently high signal-to-noise ratio for an accurate lifetime measurement. It would extend the range of the beam-laser technique if a new type of ion source were to produce more highly ionized ions (provided, of course, that the nonlinear optics extended the wavelength sufficiently far to shorter wavelengths).

In conclusion, the beam-laser technique is an effective way of measuring accurate lifetimes of the resonance levels for a singly ionized atom. Many other ions of importance in astrophysics can be studied this way. Measurements for one such ion, Fe II, are already under way in this laboratory.

BIBLIOGRAPHY

An70 T. Andersen, J. Desesquelles, K. A. Jessen and G. Sorensen, J. Quant. Spectrosc. Radiat. Transfer **10** (1970) 1143.

AP76 T. Andersen and P. Petersen, J. Quant. Spectrosc. Radiat. Transfer **17** (1977) 389.

AYP89 W. Ansbacher, Y. Li, E. H. Pinnington, Phys. Lett. **139** (1989) 165.

BBB70 H. G. Berry, J. Bromander, and R. Buchta, Physica Scripta. **1** (1970) 181.

Be69 P. R. Bevington, "Data Reduction and Error Analysis for the Physical Sciences", McGRW-HiLL, New York (1969).

BL65 N. Bloembergen, "Nonlinear Optics", Benjamin, New York (1965).

Bo68 G. D. Boyd and D. A. Kleinman, J. Appl. Phys., **39** (1968) 3597.

Co77 A. Corney, "Atomic and Laser Spectroscopy", Clarendon Press, Oxford (1977).

Da69 C. C. Davis and T. A. King, J. Phys. A: Gen. Phys. **3** (1970) 101.

De84 N. B. Delone and V. P. Krainov, "Atoms in Strong Light Fields", Springer-Verlag, Berlin (1984).

Du88 P. D. Dumont, H. P. Garnir, Y. Baudinet-Robinet and A. El Himdy Nucl. Instr. and Meth. **B35** (1988) 191.

Fi76 Charlotte Froese Fischer, Can. J. Phys. **54** (1976) 1465.

Fr61 P. A. Franken, A. E. Hill, C. W. Peters, and G. Weinreich, Phys. Rev. Lett. **7**, (1961) 118.

Ga82 A. Gaupp, P. Kuske, and H. J. Andra, Phys. Rev. **26** (1982) 3351.

Gan87 P. S. Ganas, J. Appl. Phys. **62** (1987) 1987.

Go88 R. N. Gosselin, Ph. D Thesis, University of Alberta, Edmonton, 1988.

GPA87 R. N. Gosselin, E. H. Pinnington and W. Ansbacher, Phys. Lett. **123** (1987) 175.

Gr78 P. F. Gruzdev and N. V. Afanaseva, Opt. Spectrosc., **45** (1978) 611.

Ha86 R. Hallin, A. Arnesen, C. Nordling, O. Vogel and A. Wannstrom, Vacuum, **36** (1986) 939.

Hi83 A. Hibbert, Mon. Not. R. Astr. Soc., **205** (1983) 535.

HW77 P. G. Harper and B. S. Wherrett, "Nonlinear Optics", Academic Press, London(1977).

Kl62 D. A. Kleinman, Phys. Rev. **126** (1962) 1977.

Ku78 P. Kuske, N. Kirchner, W. Wittmann and H. J. Andra, Phys. Lett. **64A** (1978) 377.

La75 C. Laughlin, M.N. Lewis, and Z. J. Horak, Astrophys. J. 197 (1975) 799.

Le87 W. R. Leo, "Techniques for Nuclear and Particle Physics Experiments", Springer-Verlag, Berlin (1987).

Lil80 L. Lilgeby, A. Lindgard, S. Mannervik, E. Vege and B. Jelenkovic, Phys. Scr. 21 (1980) 805.

Lo83 Rodney Loudon, "The Quantum Theory of Light", Clarendon Press, Oxford (1983).

Lu73 L. Lundin, B. Engman, J. Hilke and I. Martinson, Physica Scripta 8 (1973) 274.

LW73 C. Lewins and W. R. Ware, Rev. Sci. Instrum. 44 (1973) 107.

Ma88 I. Martinson, J. Opt. Soc. Am. **B5** (1988) 2159.

Ma89 I. Martinson, Rep. Prog. Phys. **52** (1989) 157.

Mi87 G. Michaud, Physica Scripta 36 (1987) 112.

MS88 W. R. MacGillivray and M. C. Standage, Physics Reports, **1** (1988) 1.

OP84 D. V. O'Connor and D. Phillips, "Time-correlated Single Photon Counting", Academic Press, London (1984).

Ra87 L. J. Radziemski, R. W. Solarv and J. A. Paisner, " Laser Spectroscopy and Its Application", Marcel Dekker, New York (1987).

Se87 A. Sen, L. S. Goodman, and W. J. Childs, Rev. Sci. Instrum. **59** (1988) 74.

Sh84 Y. R. Shen, "The Principles of Nonlinear Optics", John Wiley & Sons", New York (1984).

Si75 K. Siomos, H. Figger, and H. Walther, Z. Physik. **A 272** (1975) 355

Sim66 W. W. Smith, and A. Gallagher, Phys. Rev. **A 145** (1966) 26.

SL71 W. H. Smith and H. S. Litzt, J. Opt. Soc. Am. **B 61** (1971) 938.

So79 I. I. Sobelman, " Atomic Spectra and Radiative Transitions", Springer-Verlag, Berlin (1979).

SV81 I. I. Sobelman, L. A. Vainshtein and E. A. Yukov, " Excitation of Atoms and Broadening of Spectral Lines", Springer-Verlag, Berlin (1981).

TC88 C. E. Theodosiou and L. J. Curtis, Phys. Rev. **A 38** (1988) 4435.

Ti88 S. N. Tiwary, A. P. Singh, D. D. Singh and R. J. Sharma, Can. J. Phys. **66** (1988) 1076.

Ya75 A. Yariv, "Quantum Electronics", John Wiley & Sons, New York (1975).

Zi85 V. A. Zilitis, Opt. Spectrosc. **59** (1985) 3.

Appendix Mg II Decay Data

```
999 12 3.00 30 .02 6000. .0010 .010 .20 .40 .000  500. 0 2 1
MG89 .20 2796 2 10X 2M200U      3   25                                    0 50
MG89 .20 2796 2 10.000 1.418 3.800 0.0                                     3
  0 17354 217   7 15017 216  14 13204 209  21 11983 228  28 10207 182
 35  9224 230  42  8095 194  49  7278 202  56  6196 163  63  5567 212
 70  4943 214  77  4263 216  84  3913 230  91  3426 202  98  2990 195
105  2738 199 112  2384 198 119  2104 202 126  1750 223 133  1642 165
140  1468 229 147  1322 180 154  1250 184 161  1048 227 168   856 179
168   946 176 161  1010 178 154  1173 178 147  1213 164 140  1421 203
133  1590 205 126  1910 239 119  1912 175 112  2407 230 105  2669 169
 98  3073 173  91  3450 173  84  3904 204  77  4276 225  70  4744 216
 63  5497 208  56  6297 220  49  7009 231  42  8073 179  35  9093 199
 28 10404 198  21 11786 216  14 13204 186   7 14807 185   0 16417 182
MG89 .20 2796 3 10X 2M200U      3   29                                    0 58
MG89 .20 2796 3 10.000 1.418 3.800 0.0                                     3
  0 16590 196   8 14629 186  16 12427 192  24 11085 194  32  9561 196
 40  8188 208  48  6950 207  56  6119 208  64  5513 222  72  4445 207
 80  4060 205  88  3446 225  96  3088 192 104  2750 208 112  2252 230
120  2060 175 128  1741 215 136  1520 184 144  1374 193 152  1182 191
160  1073 217 168   896 186 176   808 214 184   655 172 192   651 199
200   669 193 208   585 228 216   495 181 224   423 213 224   472 219
216   491 180 208   561 171 200   583 199 192   738 198 184   712 194
176   911 230 168   936 186 160  1104 186 152  1263 198 144  1467 168
136  1583 183 128  1735 175 120  2067 188 112  2523 198 104  2793 216
 96  3092 214  88  3660 213  80  4054 212  72  4707 202  64  5672 187
 56  6037 198  48  7458 161  40  8219 222  32  9383 212  24 11082 218
 16 12736 220   8 14254 183   0 16462 205   0     0   0   0     0   0
MG89 .33 2796 6 10X 2M200U      3   29                                    0 58
MG89 .33 2796 6 10.000 1.629 3.8   0.0                                     3
  0 13718 201   8 12238 199  16 10642 207  24  9432 187  32  8630 201
 40  7753 238  48  6521 184  56  5848 218  64  5090 182  72  4507 199
 80  3795 216  88  3780 210  96  3282 181 104  2744 199 112  2500 229
120  2192 226 128  1874 164 136  1642 224 144  1445 192 152  1398 211
160  1140 206 168  1061 196 176   976 197 184   884 193 192   788 210
200   720 193 208   697 202 216   571 227 224   580 174 224   547 224
216   586 177 208   676 192 200   701 201 192   827 196 184   917 197
176  1022 204 168  1062 184 160  1262 215 152  1487 226 144  1455 233
136  1625 204 128  1860 198 120  2112 195 112  2335 219 104  2789 244
 96  3181 213  88  3585 174  80  3963 206  72  4372 206  64  4954 201
 56  5663 212  48  6578 249  40  7363 225  32  8247 207  24  9606 203
 16 10621 200   8 11906 222   0 13179 202   0     0   0   0     0   0
```

```
MG89 .33 2796 7 10X 1M200U      3   29                                          0 58
MG89 .33 2796 7 10.000 1.629 3.8   0.0                                          3
  0  6285  87   8  5488  80  16  4694  99  24  4319  89  32  3783  70
 40  3323  87  48  2942  93  56  2560 106  64  2245 112  72  2007  85
 80  1765  80  88  1549  86  96  1398  97 104  1195  96 112  1064  68
120   942  94 128   850  81 136   722  75 144   670  87 152   593  92
160   555  81 168   513  91 176   454  76 184   381  80 192   330  93
200   305  85 208   305  85 216   252  96 224   242  95 224   276  72
216   243  94 208   270  93 200   282  95 192   346 108 184   416  90
176   428  99 168   493  93 160   559 100 152   618 106 144   668 100
136   775 101 128   829  79 120   928  95 112  1052  81 104  1217  76
 96  1262  66  88  1583  74  80  1736  73  72  1939  84  64  2192 106
 56  2553  84  48  2913 106  40  3251  86  32  3603  76  24  4174  83
 16  4699  72   8  5534  88   0  6137  93   0     0   0   0     0   0
MG89 .33 2803 1 10X 1M200U      3   29                                          0 58
MG89 .33 2803 1 10.000 1.629 3.800 0.0                                         3
  0  4700 128   8  4321 128  16  3569 108  24  3251 104  32  2790  86
 40  2524 125  48  2368 124  56  1904 106  64  1744  92  72  1509 129
 80  1459 106  88  1233 102  96  1102  96 104   916  98 112   854 113
120   783 114 128   718 140 136   596  99 144   524 120 152   510  98
160   438 110 168   409 106 176   392 103 184   324 129 192   306  93
200   269 114 208   296 112 216   246 134 224   243 103 224   250 115
216   260 108 208   267 120 200   267 117 192   336 113 184   299  99
176   397  98 168   434 112 160   450  89 152   502 106 144   573  80
136   539 101 128   615 100 120   797 111 112   905 111 104  1011  99
 96  1168 103  88  1279 115  80  1274  98  72  1668 104  64  1654  87
 56  2090 107  48  2128 108  40  2469 114  32  2866 119  24  3244 108
 16  3551 117   8  4079 123   0  4718 104   0     0   0   0     0   0
MG89 .33 2803 2 10X 1M200U      3   29                                          0 58
MG89 .33 2803 2 10.000 1.629 3.800 0.0                                         3
  0  7607 117   8  6935 133  16  5687 141  24  5237 134  32  4454 116
 40  4041 123  48  3647 128  56  3162 141  64  2652 145  72  2330 104
 80  2248 132  88  1835 122  96  1768 126 104  1520 130 112  1366 143
120  1234 120 128  1060 104 136   993 130 144   914 133 152   746 100
160   711 113 168   611  95 176   524 128 184   461 125 192   469 135
200   385 114 208   438 147 216   376 125 224   345 104 224   304 122
216   334 127 208   350 124 200   486 140 192   443 118 184   414 139
176   517 128 168   591 109 160   736 115 152   775 152 144   923 133
136   996 132 128  1098 125 120  1196 114 112  1366 110 104  1501  91
 96  1690 126  88  1897 136  80  2176 141  72  2489 144  64  2592 122
 56  3026 133  48  3511 116  40  3890 131  32  4563 129  24  5123 107
 16  5671 115   8  6131 119   0  7425 124   0     0   0   0     0   0
```

```
MG89 .33 2803 3 10X 1M200U      3   29                                          0 58
MG89 .33 2803 3 10.000 1.629 3.800 0.0                                          3
  0  7416 166   8  6726 150  16  5670 134  24  5208 116  32  4442 121
 40  3959 123  48  3756 129  56  3152 124  64  2723  96  72  2318 120
 80  2149 120  88  1933 140  96  1573 123 104  1547 112 112  1298 131
120  1183 112 128  1073 134 136   973 136 144   854 120 152   735 119
160   737 142 168   581 107 176   589 140 184   547 137 192   448 132
200   441 132 208   356 102 216   390 108 224   320 128 224   342 112
216   333  97 208   424 113 200   453 120 192   436 135 184   482 119
176   552 132 168   579 119 160   747 136 152   739 114 144   842  88
136  1003 158 128  1176 131 120  1234 127 112  1351 143 104  1629 146
 96  1743 131  88  1970 123  80  2087 132  72  2614 131  64  2674 135
 56  3494 138  48  3644 157  40  3957 106  32  4696 122  24  5251 149
 16  6009 124   8  6566 139   0  7455 112   0     0   0   0     0   0
MG89 .33 2803 4 10X 1M200U      3   29                                          0 58
MG89 .33 2803 4 10.000 1.629 3.800 0.0                                          3
  0  8060 114   8  7116 129  16  6443 139  24  5848 152  32  5036 141
 40  4296 134  48  4039 100  56  3432 179  64  3084 133  72  2730 133
 80  2342 124  88  2101 133  96  1900 153 104  1659 130 112  1498 151
120  1444 159 128  1233 139 136  1062 137 144   976 137 152   805 111
160   833 158 168   677 144 176   626 136 184   554 139 192   482 105
200   449 141 208   412 165 216   386 135 224   325 157 224   372 146
216   356  99 208   448 132 200   438 134 192   491 148 184   525 122
176   610 118 168   673 145 160   766 128 152   851 131 144   944 116
136  1080 131 128  1252 151 120  1386 147 112  1482 120 104  1710 146
 96  1865 142  88  2173 135  80  2444 148  72  2675 125  64  3117 148
 56  3590 129  48  4034 139  40  4306 111  32  4993 175  24  5555 132
 16  6626 133   8  7073 142   0  8225 131   0     0   0   0     0   0
MG89 .20 2803 5 10X 1M200U      4   29                                          0 58
MG89 .20 2803 5 10.000 1.418 3.800 0.0                                          3
  0 14151 217   8 15393 233  16 14697 193  24 13278 217  32 11473 215
 40 10235 199  48  8869 210  56  7570 249  64  6658 201  72  5717 210
 80  5087 183  88  4270 188  96  3753 184 104  3285 203 112  2897 218
120  2382 216 128  2301 200 136  1851 207 144  1605 196 152  1567 169
160  1279 191 168  1172 177 176  1061 201 184   884 170 192   800 174
200   798 240 208   618 166 216   557 184 224   473 204 224   502 189
216   610 185 208   664 190 200   744 202 192   734 200 184   908 183
176   974 187 168  1136 220 160  1323 176 152  1385 218 144  1671 179
136  1857 172 128  2167 211 120  2453 172 112  2781 173 104  3288 225
 96  3713 221  88  4467 172  80  5034 195  72  5683 243  64  6640 180
 56  7465 199  48  8835 215  40  9819 177  32 11447 186  24 13399 212
 16 14577 191   8 15180 221   0 14693 214   0     0   0   0     0   0
```